Impact of Cloud Model Microphysics on Passive Microwave Retrievals of Cloud Properties. Part I: Model Comparison Using EOF Analyses

MICHAEL I. BIGGERSTAFF AND EUN-KYOUNG SEO

School of Meteorology, University of Oklahoma, Norman, Oklahoma

SVETLA M. HRISTOVA-VELEVA

Jet Propulsion Laboratory, Pasadena, California

KWANG-YUL KIM

The Florida State University, Tallahassee, Florida

(Manuscript received 11 August 2004, in final form 2 September 2005)

ABSTRACT

The impact of model microphysics on the relationships among hydrometeor profiles, latent heating, and derived satellite microwave brightness temperatures T_B have been examined using a nonhydrostatic, adaptive-grid cloud model to simulate a mesoscale convective system over water. Two microphysical schemes (each employing three-ice bulk parameterizations) were tested for two different assumptions in the number of ice crystals assumed to be activated at 0°C to produce simulations with differing amounts of supercooled cloud water. The model output was examined using empirical orthogonal function (EOF) analysis, which provided a quantitative framework in which to compare the simulations. Differences in the structure of the vertical anomaly patterns were related to physical processes and attributed to different approaches in cloud microphysical parameterizations in the two schemes. Correlations between the first EOF coefficients of cloud properties and T_B at frequencies associated with the Tropical Rainfall Measuring Mission (TRMM) Microwave Imager (TMI) showed additional differences between the two parameterization schemes that affected the relationship between hydrometeors and T_B. Classified in terms of T_B, the microphysical schemes produced significantly different mean vertical profiles of cloud water, cloud ice, snow, vertical velocity, and latent heating. The impact of supercooled cloud water on the 85-GHz T_B led to a 15% variation in mean convective rain mass at the surface. The variability in mean profiles produced by the four simulations indicates that the retrievals of cloud properties, especially latent heating, based on TMI frequencies are dependent on the particular microphysical parameterizations used to construct the retrieval database.

1. Introduction

Latent heat released by precipitation in the tropical atmosphere, which accounts for nearly two-thirds of the global rainfall (Simpson et al. 1988; Tao et al. 1993), is an important energy source for driving large-scale circulations (e.g., Riehl and Malkus 1958; Malkus 1962; Riehl and Simpson 1979). Measurements of precipitation can help to provide an estimate of vertically integrated latent heat release (Houze 1982). Tropical precipitation is difficult to measure, however. The standard deviation of monthly rainfall is comparable to the mean value (Thiele 1987). Moreover, given the distribution of land, precipitation cannot be directly measured over the entire area.

To overcome the difficulty in taking direct measurements of rainfall in the Tropics, satellite-based observations have been used to infer rainfall from the cloud-top temperatures (e.g., Adler and Negri 1988), radar backscattering (Iguchi et al. 2000; Meneghini et al. 2004), or microwave emissions from the cloud and precipitation field (Wilheit et al. 1977, 1982; Spencer et al. 1983; Wu and Weinman 1984; Spencer 1986). The

Corresponding author address: Dr. Michael Biggerstaff, School of Meteorology, University of Oklahoma, 100 E. Boyd Street, SEC Rm. 1310, Norman, OK 73019.
E-mail: drdoppler@ou.edu

passive microwave techniques relate brightness temperatures T_B representative of the upwelling radiances resulting from interactions between microwave energy emitted by the surface and the hydrometeors in clouds, to path-integrated rainfall. For example, neglecting the contribution from the atmospheric thermal structure and considering measurements taken over uniform and radiometrically cold surfaces (such as the ocean), T_B associated with low microwave frequencies (less than 20 GHz) are likely to be from thermal emissions attributed to liquid water in clouds (Wilheit et al. 1977; Wilheit 1986). The T_B associated with higher microwave frequencies (37 GHz and higher) are affected by scattering by large ice particles (Wilheit et al. 1982; Spencer et al. 1983, 1989; Wu and Weinman 1984; Spencer 1986; Smith et al. 1992). Hence, a combination of low and high frequencies provides insight to the vertical structure of hydrometeors from which surface rainfall can be estimated.

Simpson et al. (1988) suggested that cloud dynamical–microphysical models in conjunction with a radiative transfer model could provide a consistent framework in which to relate microwave measurements to cloud properties. Databases from numerical simulations of convective storm systems have been built to relate snapshots of T_B to cloud microphysical properties (e.g., Adler et al. 1991; Smith et al. 1992; Mugnai et al. 1993; Tao and Simpson 1993; Kummerow et al. 1996). Using these databases, rainfall and vertical profiles of hydrometeors and latent heating have been retrieved by inverting the observed radiances from satellite instruments using profiling inversion algorithms (e.g., Smith et al. 1994; Kummerow et al. 1996; Olson et al. 1996, 1999).

Errors in the retrieved properties arise from both uncertainties in the assumed physical relationships between the measured and retrieved quantities and uncertainties associated with statistical methods employed in the retrieval. One difficulty in using a set of microwave T_B to estimate rainfall is the nonunique relationship between T_B and the vertical distribution of hydrometeors in clouds (Twomey 1977). Indeed, Petty (1999) used a one-dimensional cloud model to show that many different hydrometeor profiles could produce the same set of T_B. Profiling inversion algorithms are also dependent on the databases used to perform the retrieval. Panegrossi et al. (1998) noted that cloud models produce very different manifolds (multidimensional distributions) in brightness temperature space depending on the environmental conditions used to initialize the models. They stressed the need for similar characteristics between the observed and model-derived T_B databases to provide numeric stability in profiling inversion algorithms. Smith et al. (1992) further suggested that T_B–rain rate relations based on numerical simulations are sensitive to the sophistication of the model microphysical parameterization scheme. They indicated that this sensitivity should be a greater concern than the level of sophistication used in the radiative transfer model.

It seems clear that the implementation of the microphysical scheme used in a cloud model might also have significant influence on the retrieval of microphysical variables from passive microwave observations. Taking into account the comments of Smith et al. (1992), Hristova-Veleva (2000) conducted a set of numerical simulations to examine the uncertainty in T_B–rain rate relations. She modified two very similar microphysical schemes to eliminate differences in the descriptive parameters that McCumber et al. (1991) found to have the greatest effect on simulated storm structure. A set of experiments were then conducted to evaluate the impact of supercooled cloud water on the T_B–rain rate relations as well as to determine whether differences in the philosophies behind the two parameterization schemes led to differences in the T_B–rain rate relations. Supercooled cloud water had already been identified by Adler et al. (1991) as reducing the minima in T_B at high frequencies, associated with scattering by high-density ice particles, by absorbing the scattered energy and reemitting it in the direction of the satellite. Comparing the results from two implementations of similarly designed microphysical parameterizations provides an additional check on whether the results are dependent on a particular scheme.

In this paper, we use empirical orthogonal function (EOF) analysis to quantitatively evaluate the differences in the storms simulated by Hristova-Veleva (2000) and to compare the model output as a function of brightness temperatures at frequencies associated with the Tropical Rainfall Measuring Mission (TRMM) Microwave Imager (TMI; Kummerow et al. 2000). The EOF analyses reveal the vertical structure of the variance in the distribution of individual cloud properties. Hence, EOF analyses provide a method to determine whether two simulations are producing clouds with structurally different perturbations from the mean vertical profile of a cloud property. This investigation can provide insight to the role of physical processes within the model on cloud hydrometeor distributions. The EOF framework also allows for the determination of the correlation between T_B and cloud properties such as surface rainfall and latent heating.

We find that systematic differences in microphysical parameterizations tested in the cloud model led to different anomaly patterns that could be attributed to

TABLE 1. Parameterization scheme and selected microphysical parameter settings for the simulations used in this study. NCIO is the assumed number of activated cloud-ice nuclei at 0°C. EIS and ESG are the collection efficiencies for snow removing ice and graupel removing snow, respectively.

Model run	Origin of parameterization	NCIO (m^{-3})	EIS	ESG
Scheme A, moderate efficiencies, low ice (AM_eL_i)	Tao and Simpson (1993)	10^{-2}	0.1	0.1
Scheme B, moderate efficiencies, low ice (BM_eL_i)	Keenan et al. (1994)	10^{-2}	0.1	0.1
Scheme A, moderate efficiencies, high ice (AM_eH_i)	Tao and Simpson (1993)	10^{7}	0.1	0.1
Scheme B, moderate efficiencies, high ice (BM_eH_i)	Keenan et al. (1994)	10^{7}	0.1	0.1

physical processes. When the hydrometeor profiles were classified in terms of brightness temperatures, the microphysical schemes produced significantly different mean profiles of cloud water, cloud ice, snow, vertical velocity, and latent heating. The EOF analysis showed that these cloud properties were poorly correlated to brightness temperature. Over convective regions, surface rain mass classified by 85-GHz T_B varied by about 15% depending on the microphysical parameterization used in the cloud model.

The results presented here indicate that model microphysics is an important source of uncertainty in retrievals of latent heating from passive microwave observations and also contributes to the uncertainty in rain retrievals, particularly over land where high surface emissivity results in only the 85-GHz T_B providing useful information. In a companion paper, Seo and Biggerstaff (2006, hereinafter Part II) show that the impact of model microphysics on the retrieval of latent heating can be greater than the inherent uncertainty resulting from the nonuniqueness in T_B–latent heating relations.

2. Data sources

a. Models in use

1) CLOUD MODEL

The EOF analysis was conducted on output from four of the six simulations described in Hristova-Veleva (2000). Those simulations were performed with the Collaborative Model for Multiscale Atmospheric Simulation (COMMAS; Skamarock and Klemp 1993) initiated with an environmental sounding conducive to the development of a leading-line trailing-stratiform squall line system (Houze et al. 1990; Biggerstaff and Houze 1991a,b). Squall lines represent a common mode of convective organization for mesoscale convective systems in midlatitudes (Houze et al. 1989; Hashem and Biggerstaff 1997) and the Tropics (e.g., Zipser 1969, 1977). The initialization procedure for this simulation follows that in Skamarock et al. (1994).

The microphysical parameterization schemes used in the model are variants of Lin et al. (1983), taken from Tao and Simpson (1993), and of Rutledge and Hobbs (1984), taken from Keenan et al. (1994). These bulk microphysical schemes employ parameterizations for two classes of liquid water (cloud water and rain) and three classes of ice (cloud ice, snow, and graupel). A more detailed description of the microphysical schemes and model initialization procedures can be found in Hristova-Veleva (2000).

Here we make use of the four simulations that have temperature-independent collection efficiencies for graupel-collecting snow and snow-collecting cloud ice (Table 1). These four simulations span the range of variability found in Hristova-Veleva's (2000) six simulations. They are referred to as AM_eH_i, AM_eL_i, BM_eH_i, and BM_eL_i, where the first character indicates the particular variant of the parameterization scheme [A for those based on a graupel version of Tao and Simpson (1993), and B for those based on the scheme used in Keenan et al. (1994)]. The second character, with subscript "e," refers to the temperature-independent collection efficiencies that were set equal in all four simulations used here. The third character, with subscript "i" denotes the value of the assumed number of activated ice crystals at 0°C (the so-called NCIO parameter), with L_i representing a value of 10^{-2} m^{-3} and H_i representing a value of 10^{7} m^{-3}. The first value was chosen to represent environments that support accumulation of supercooled cloud water, like midlatitudes with high concentrations of cloud condensation nuclei, where cloud water is distributed over a large number of small particles that can be carried aloft in the convective updrafts. The latter value was set artificially high to ensure that the condensed water vapor would be assigned to cloud ice rather than cloud water in the simulation. This procedure was done to represent environments that produce clouds with little supercooled cloud water, like tropical oceanic regimes and the Amazon (e.g., Stith et al. 2002). Hence, the AM_eH_i (BM_eH_i) versus AM_eL_i (BM_eL_i) comparisons allow for examination of the impact of supercooled cloud water on relationships between brightness temperatures and cloud properties. In a similar way, the AM_eH_i (AM_eL_i) versus BM_eH_i (BM_eL_i) comparisons allow for examination of the sensitivity of the results to a particular implementation of the microphysical parameterizations.

2) RADIATIVE TRANSFER MODEL

Microwave brightness temperatures are calculated from the hydrometeor profiles produced in the cloud model using a one-dimensional Eddington's-second-approximation radiative transfer model (Weinman and Davies 1978; Kummerow 1993). For rain, snow, and graupel, an exponential drop size distribution was used (Marshall and Palmer 1948). The densities of snow and graupel were 100 and 400 kg m^{-3}, respectively, and the intercepts of rain, snow, and graupel were 8×10^6, 3×10^6, and 4×10^6 m^{-4}, respectively. For radiative transfer calculations cloud water and cloud ice particles are assumed to be monodispersed, 20-μm-diameter spheres. Mie theory (Mie 1908) is employed for computing all single-particle scattering properties.

Brightness temperatures were calculated at 10, 19, 21, 37, and 85 GHz, the same as the TMI channels. Nadir viewing has been assumed for simplicity. Direct application to satellite measurements would require taking into account the specific geometry of the instrument and the orbit of the satellite.

b. Simulations and model data

All model-generated variables, including microphysical mass contents in a unit volume (densities), latent heat release, and vertical velocity, were archived. The model output during the mature stage (Leary and Houze 1979) of the simulated storm (from 6 to 7.5 h) was sampled at 6×6 km^2 horizontal resolution and 700-m vertical resolution, with a temporal resolution of 5 min. Radar reflectivity was calculated from the hydrometeor fields under an assumption of Rayleigh scattering. All precipitation points in the dataset were classified into either convective or stratiform following the procedure of Tao and Simpson (1993). The precipitation classification is important in understanding microphysical processes (Houghton 1968; Biggerstaff and Listemaa 2000) and latent heating profiles (Johnson 1984; Houze 1989).

About 10 000 vertical profiles were taken through each convective and stratiform cloud during the mature stage of each simulated storm system to create the database used here.

3. The EOF method

All of the vertical profiles of hydrometeors, vertical motion, and latent heating taken during the mature stage of the simulated squall line were combined into a single database for each microphysical parameterization scheme. To characterize the variability of the model fields and to relate scalar quantities like brightness temperatures to vector quantities like hydrometeor profiles, EOF analysis was used. EOF analysis yields the vertical structure of the variance in each model field in a way that retains information regarding the correlation between variability at different altitudes. This information is needed because each level is connected dynamically, thermodynamically, and microphysically to every other level. Although EOF analyses have been used before to diagnose and validate numerical simulations (Ferranti et al. 1994; Wang and Rui 1996; Molteni and Buizza 1999), it is worthwhile to describe the fundamental aspects and advantages in using this mathematical framework. Additional details of EOF analyses may be found in K. Y. Kim and G. R. North (1997, unpublished manuscript) and von Storch and Zwiers (1999).

a. Fundamentals of EOF analysis

If the model database is expanded in EOF space, patterns of simultaneous variation can be identified. For example, if $X_i(z)$ represents a variable (e.g., graupel content) in the vertical direction z at location i, and $\overline{X}(z)$ represents the vertical profile of the horizontally averaged mean, then the difference between $X_i(z)$ and $\overline{X}(z)$ at a given spatial location would be an anomaly $X_i'(z)$. These anomalies are then expanded on an EOF space such that

$$X_i'(z) = \sum_{j=1}^{N} A_{i,j}\phi_j(z), \tag{1}$$

where N represents the number of EOFs, $A_{i,j}$ represents the EOF coefficients, and $\phi_j(z)$ represents the EOFs. The number of EOFs N may be the number of vertical layers or fewer. Such an expansion is unique because EOFs constitute a complete set of basis functions. The EOF coefficients $A_{i,j}$ are obtained by simply projecting the anomalies $X_i'(z)$ onto the jth EOF $\phi_j(z)$.

An individual profile of a cloud property at a point in space can be reconstructed by taking the summation in (1) and adding it to the horizontally averaged vertical profile of that cloud property. One of the advantages of EOF analyses is that a good approximation to an individual profile can be reconstructed from just the mean plus the sum of the dominant EOFs. EOFs with small coefficients can be neglected.

b. Utility of the EOF analysis method

1) RETRIEVING VERTICAL PROFILES OF CLOUD PROPERTIES

Because EOFs provide multilayered relations, they can be used to constrain the retrieval of hydrometeor

profiles from a set of T_B. In the EOF framework, the content of one species cannot be arbitrarily adjusted at one level to provide a match between observed and model-derived T_B. Instead, the entire vertical profile would be adjusted based on the variance of the species in the model database. Hence, the EOF technique is an efficient way to obtain an initial guess of hydrometeor profiles from a set of T_B and provides a physical basis for perturbing the profile during retrieval. Part II uses the multilayered EOF relations developed here to assess the uncertainty of retrieved quantities to changes in the brightness temperatures.

Because the structure of the variance is represented by the EOFs $\phi_j(z)$, the dimensionality of individual profiles related to the jth EOF can be reduced to point values, the EOF coefficients. Coefficients are convenient in computing statistics such as the correlation between the vertical distribution of hydrometeors and T_B. This technique allows for a quantitative description of the differences in the hydrometeor–T_B relations associated with the four microphysical schemes examined here.

2) EOF COEFFICIENTS VERSUS VERTICALLY INTEGRATED QUANTITIES

Although the vertical *structures* of hydrometeors are closely related to T_B, the relationships in previous studies have been shown with vertically integrated quantities (e.g., Adler et al. 1991; Smith et al. 1992; Panegrossi et al. 1998). This approach basically ignores the vertical distribution of hydrometeors. EOF analysis, on the other hand, retains the dominant vertical variation of a hydrometeor profile in the first EOF while providing a proxy for the vertically integrated mass content of the hydrometeor, the coefficient for the first EOF. The greater the first EOF coefficient is, the greater is the vertically integrated mass content of the hydrometeor. This point is illustrated in Fig. 1, which shows a comparison between scatterplots generated by graphing integrated mass contents of rain and graupel as a function of T_B and scatterplots of the first EOF coefficients of rain and graupel profiles against the same T_B. As expected, 10 GHz is more closely related to rain than to graupel. Higher frequencies (37 and 85 GHz here) are more closely related to graupel than to rain.

Comparing this figure with Figs. 6–9 in Adler et al. (1991), Fig. 7 in Smith et al. (1992), and Figs. 4a, c and 5 in Panegrossi et al. (1998) suggests that the EOF coefficients can be used in place of columnar (integrated) quantities. This allows retention of the vertical hydrometeor profile structure, which can be related to the distribution of T_B. For example, the integrated columnar graupel relations do not capture as much of the scattered points at 85 GHz because the warming effect associated with cloud water depends on the relative vertical location of the supercooled cloud water and graupel. The effect of supercooled cloud water on T_B relations is better emphasized by the EOF analysis because the EOF contains the fundamental variation in the vertical structure of the profile and is a more sensitive indicator of cloud water aloft than an integrated "columnar" quantity.

4. Macroscale overview of simulated storm structure

Before employing the EOF analysis, we first examine the macroscale characteristics of the simulated storms to determine the impact of the model microphysics on bulk properties such as storm scale and mean vertical structure. This examination provides insight to the physical processes that are responsible for the different anomaly patterns that emerge from the EOF analysis.

a. Horizontal structure of the cloud systems

For each microphysical scheme, the simulation produced a mature squall line with a stratiform precipitation region trailing behind a leading convective line (Fig. 2). The 85-GHz field shows a slight reduction in T_B above the stratiform region and pronounced minima in the convective cores. These features are associated with the presence of graupel, even in the simulated stratiform rain region. While true stratiform clouds in leading-line trailing-stratiform squall line systems may contain limited amounts of graupel, simulated clouds based on three-ice microphysical parameterizations are inherently limited in the variety of ice particle densities that can be represented. As a result, snow is often given a relatively low density that allows the particles to advect over mesoscale regions as they slowly fall. This approach limits the amount of surface rain that can be produced from melting snow. On the other hand, graupel is assigned a density to allow for limited horizontal advection but a fast enough fall speed to generate surface rain immediately behind the convective region. Thus, melting graupel, rather than melting snow, generally dominates simulated stratiform rain in models that use three-class ice parameterizations. This situation leads to a greater scattering signature at 85 GHz than would be observed in stratiform regions dominated by snow. It is important to note that the actual cloud model database used in TRMM also relies on a three-class ice parameterization scheme.

Although each simulation produced the same type of storm system, there is a noticeable disparity in the be-

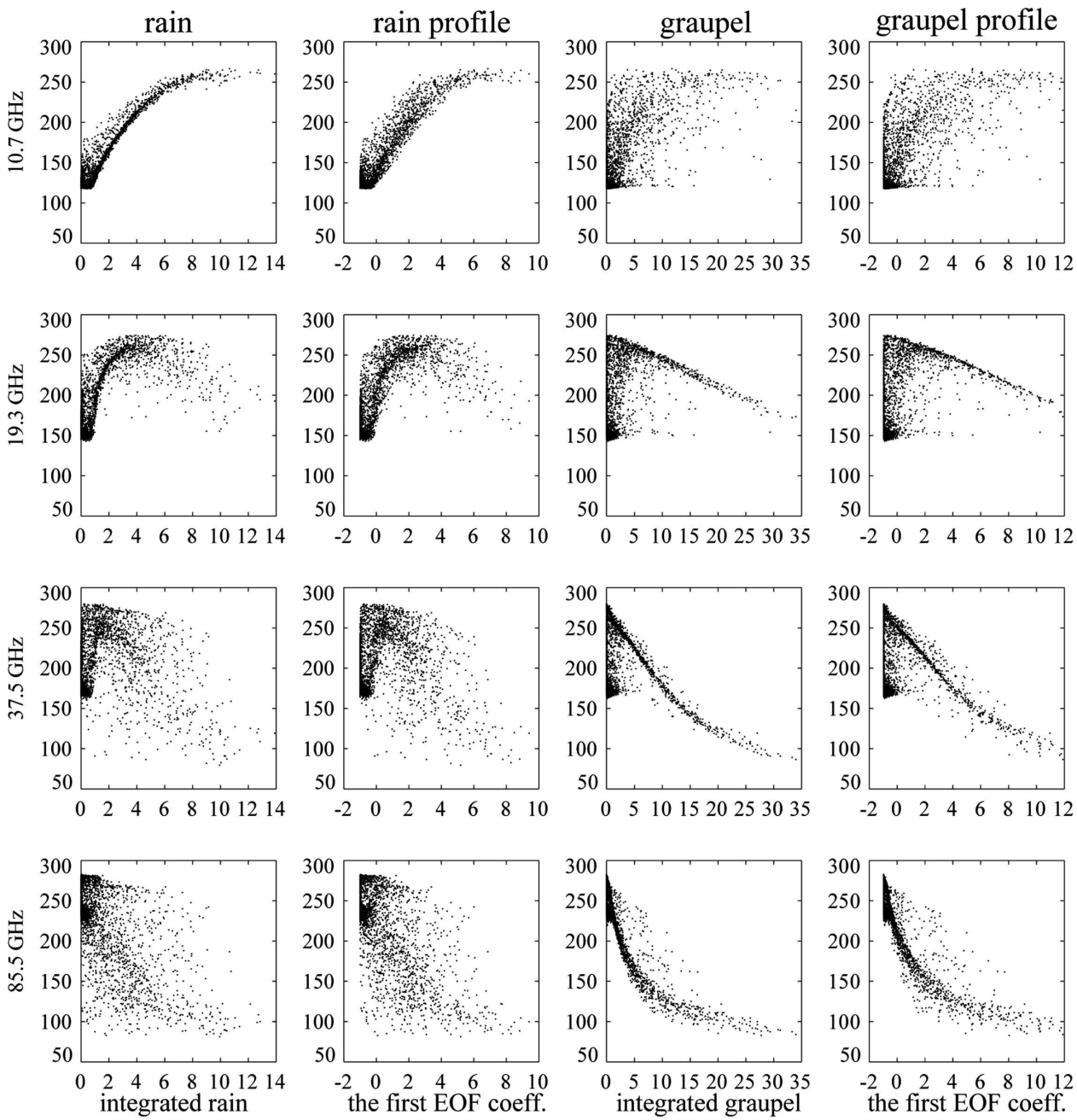

FIG. 1. Correlation diagrams between (from top row to bottom row) the four TMI T_B frequencies and (from left column to right column) vertically integrated rain (kg m^{-2}), the first EOF of the rain profile, vertically integrated graupel content (kg m^{-2}), and the first EOF of the graupel profiles for the AM_eL_i convective region.

havior of scheme B relative to scheme A in terms of the horizontal scale of the cloud system. Whereas the assumed concentration of activated ice crystals at 0°C (NCIO) had little impact on the horizontal structure of the simulations using scheme A, the low-ice run for scheme B (BM_eL_i) produced a storm system that was about 20% smaller in scale than the other three simulations. This difference was mostly due to the restricted size of the stratiform rain region in the BM_eL_i simulation. As noted by Hristova-Veleva (2000), cloud ice in scheme A is produced through a saturation-adjustment procedure in a manner that is fairly independent of the value chosen for NCIO, whereas in scheme B the production of cloud ice is more closely tied to NCIO. Thus,

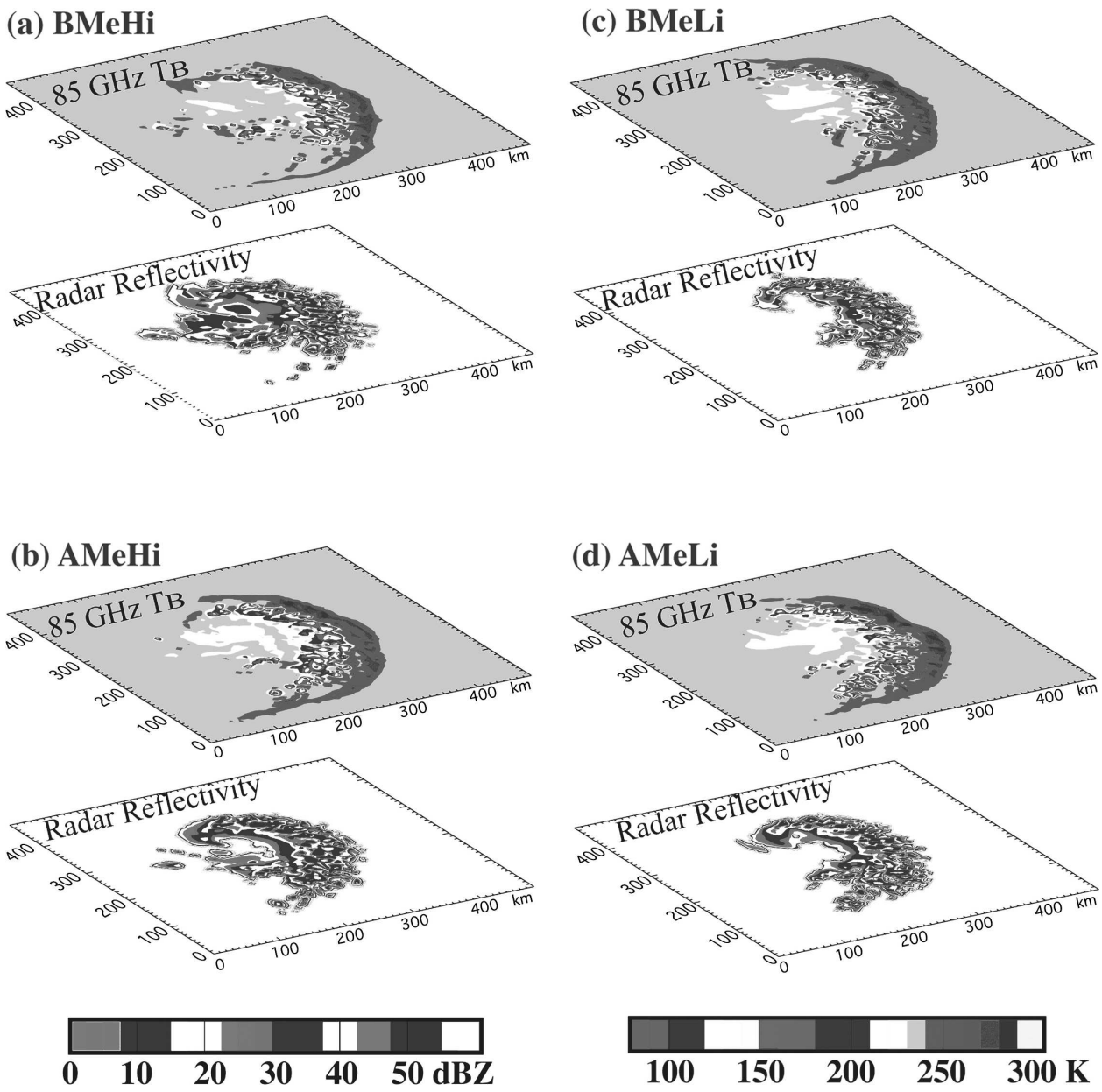

FIG. 2. The calculated T_B (top slice) at 85 GHz and model-derived radar reflectivity (bottom slice) at 3.75 km AGL at 7 h into the simulations for the (a) BM_eH_i, (b) AM_eH_i, (c) BM_eL_i, and (d) AM_eL_i microphysical schemes. The scales for T_B (K) and radar reflectivity (dBZ) are as shown. Horizontal domain size in this plot is 450×450 km^2.

philosophical choices in how the cloud-ice parameterization was implemented led to different sensitivities to changes in NCIO between the two microphysical schemes.

b. Mean vertical structure of the simulated storms

Frequently, simulated storms are compared with observations using radar reflectivity factor Z, which is readily available from weather radars and represents the sum of the sixth power of diameters of the water equivalent drops for each hydrometeor per unit volume of air (Battan 1973). Because the water equivalent diameter is used, low-density snow particles yield less radar reflectivity than high-density graupel particles of the same frozen size. Note also that the model does not distinguish between wet and dry ice. We assumed that the ice was dry until the temperature became warmer than 0°C. This assumption affects the assumed refractive index, which is taken to be the value for ice at temperatures below freezing and the value of water at

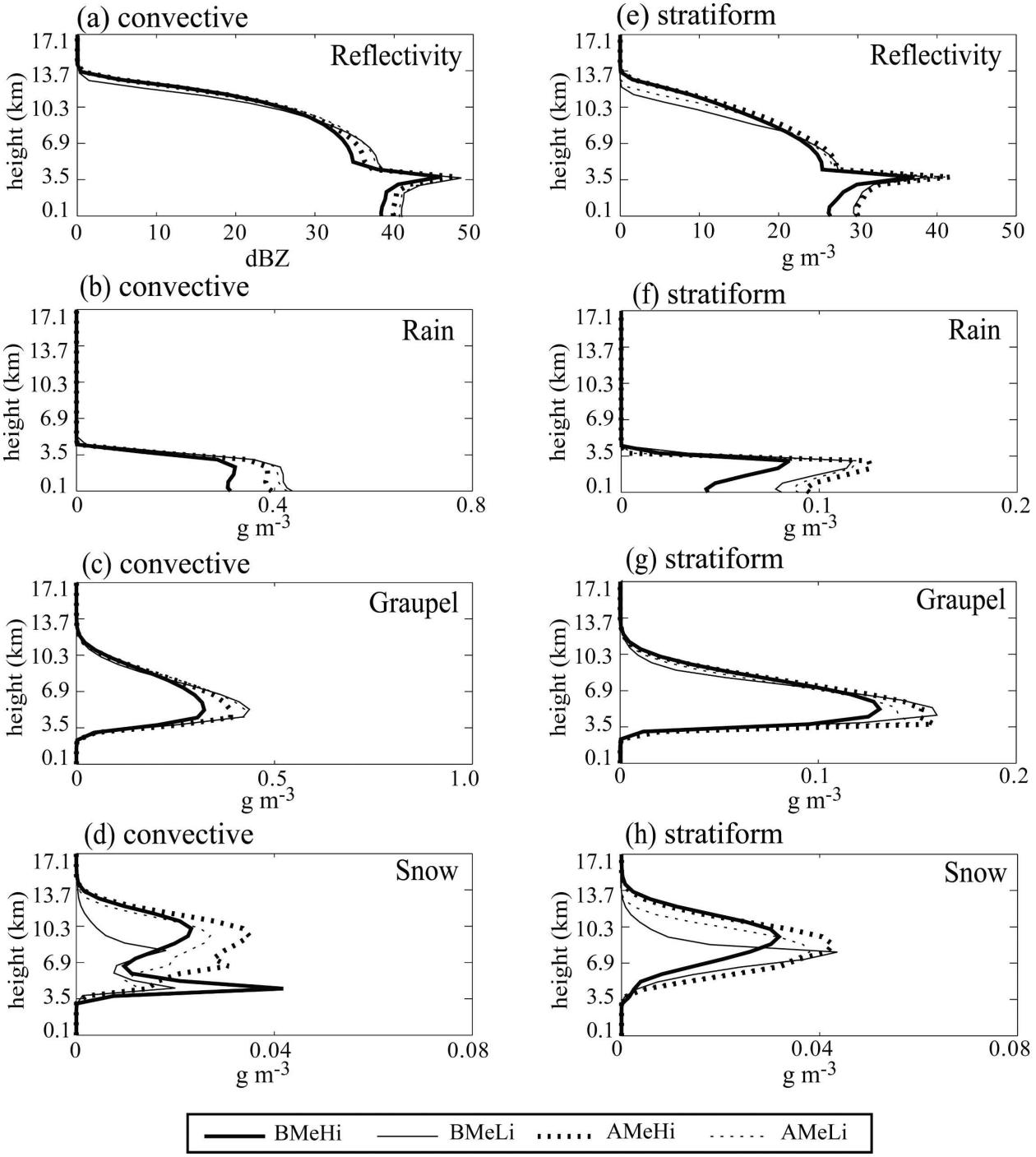

FIG. 3. Mean vertical profiles of (a), (e) radar reflectivity, (b), (f) rain, (c), (g) graupel, and (d), (h) snow at the mature stage of the simulated storm system for the (left) convective and (right) stratiform regions. Solid (dashed) lines are for the scheme-B (scheme A) simulations, with thick (thin) patterns denoting runs with high (low) ice.

warmer temperatures. Hence, the radar brightband effect associated with melting ice particles (Austin and Bemis 1950) is exaggerated in the convective region.

The four simulations exhibit very similar mean profiles of radar reflectivity over both the convective and stratiform rain regions (Fig. 3). Even though the horizontal scale of the BM_eL_i run was smaller than that for the other simulations, the liquid and high-density ice

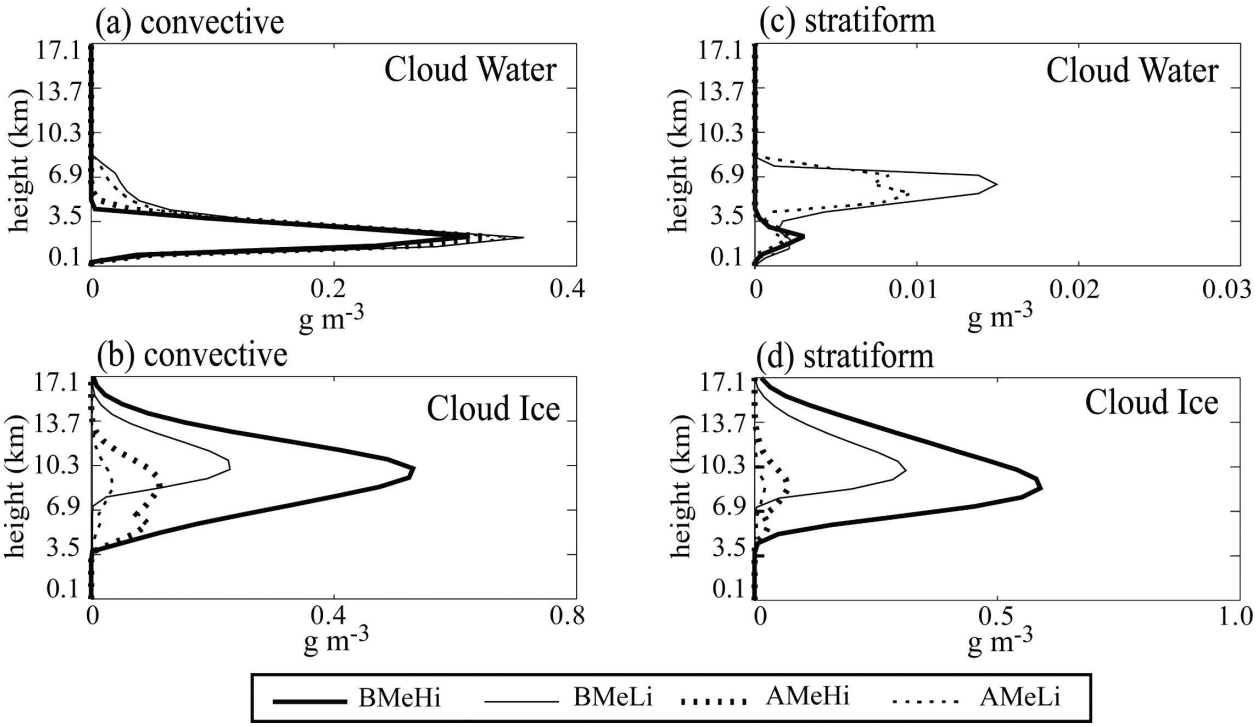

FIG. 4. Vertical profiles of mean cloud water and mean cloud ice at the mature stage of the simulated storm system for the (a), (b) convective and (c), (d) stratiform regions. Solid (dashed) lines are for the scheme-B (scheme A) simulations, with thick (thin) patterns denoting runs with high (low) ice.

precipitation that was present had similar vertical structure to that of the simulations using scheme A.

However, the BM_eH_i simulation has weaker reflectivity below the melting level (3.5-km altitude) than do the other simulations. This result is attributed to less mean rainfall that corresponded to less graupel aloft (Fig. 3). Despite having relatively high values of snow (Fig. 3d) from which graupel could form, the high-ice simulation using scheme B generated weaker accumulations of graupel and less surface rainfall on average than the other three simulations. The lack of supercooled cloud water (Fig. 4) apparently limited the production of graupel in scheme B's implementation of the microphysical parameterizations. In contrast, scheme A was mostly insensitive to the amount of supercooled cloud water.

Hristova-Veleva (2000) noted that scheme B converts cloud ice to snow through the Bergeron process only if cloud water is present. The Bergeron process accounts for the lower saturation vapor pressure over ice as compared with water such that cloud ice will grow into snow at the expense of cloud water in the mixed-phase region of the cloud (Bergeron 1935). In scheme A, the growth of ice particles into snow does not depend on the presence of supercooled cloud water (Hristova-Veleva 2000). This fact also explains the dramatic differences in accumulated cloud ice among the four simulations (Fig. 4). Again, philosophical differences in how the microphysical parameterizations were implemented led to a dichotomy in sensitivity of the two schemes to the NCIO parameter.

5. Results from the EOF analysis

a. Variability patterns from the EOF analysis

EOF analyses were conducted to determine quantitatively how similar the cloud structures were among the four simulations. EOF analysis was performed for the anomalies from the mean vertical profile of each parameter in the database. For radar reflectivity, the linear equivalent radar reflectivity factor (Z_e; mm^6 m^{-3}) was used during the EOF analysis, mean, and standard deviation, and the results were converted to logarithmic units (dBZ) for display. Results from the EOF analysis are illustrated for vertical velocity, latent heating, and snow (Figs. 5, 6).

The structure of the EOF is related to physical processes within the clouds. For example, the first EOF of vertical velocity profiles over the convective region is associated with net upward motion at all levels and represents both the variability in strength of convective drafts in mature cells and the net upward motion in

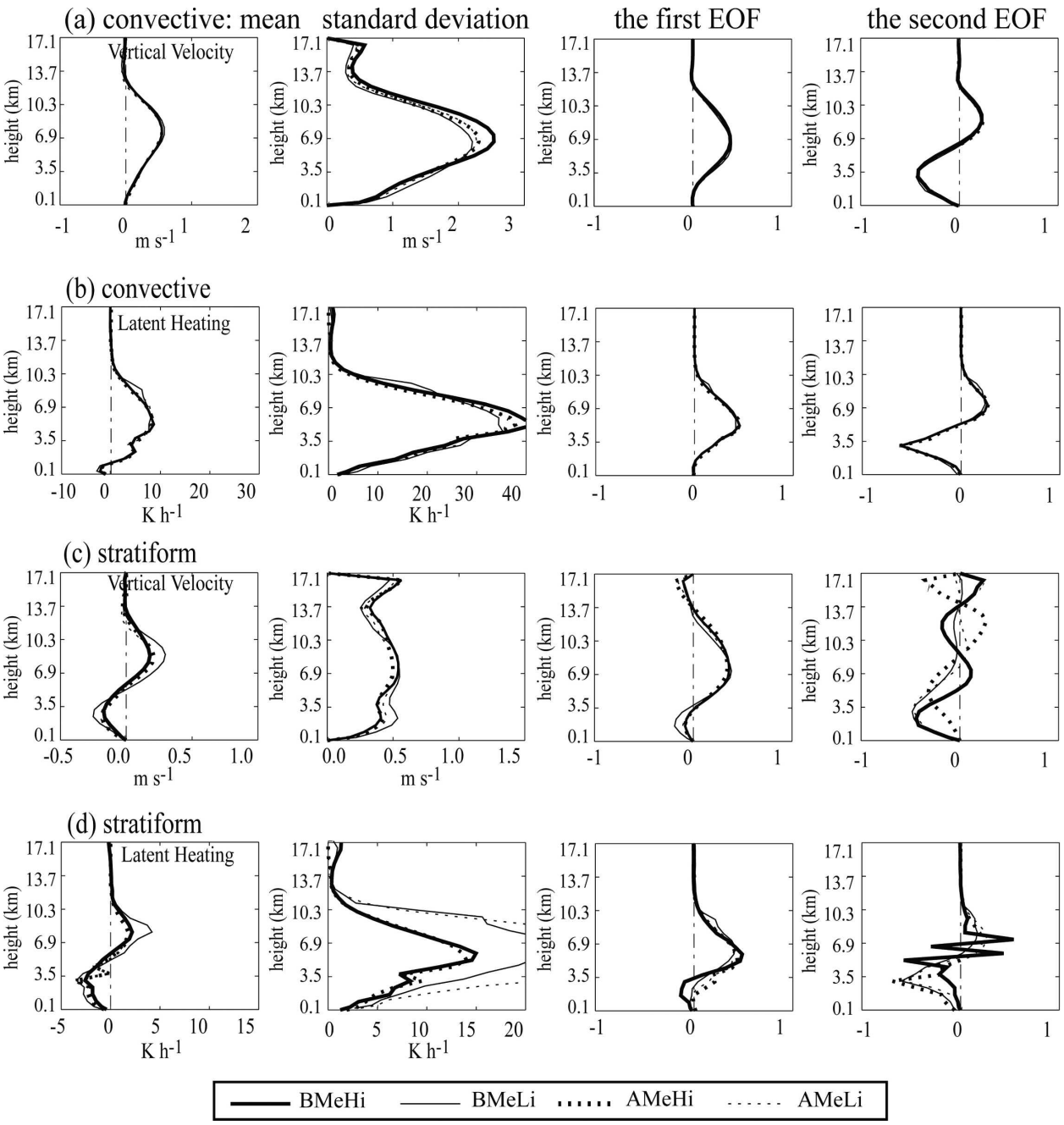

FIG. 5. Vertical profiles of (from left column to right column) the mean, the standard deviation, and the two dominant EOFs of (a) vertical velocity (m s^{-1}) and (b) latent heating (K h^{-1}) in the convective region and (c) vertical velocity (m s^{-1}) and (d) latent heating (K h^{-1}) in the stratiform region. Solid (dashed) lines are for the scheme-B (scheme A) simulations, with thick (thin) patterns denoting runs with high (low) ice.

developing convective cells. The second EOF in vertical velocity represents convective downdrafts at lower levels in conjunction with slightly weaker updrafts at upper levels, which are typical of mature-to-dissipating convective cells (Byers and Braham 1949).

For the convective region (Figs. 5a,b), not only are the mean and standard deviations of the vertical velocity and latent heating similar, so are the vertical variability patterns as represented by the first and second EOF. Thus, in terms of these parameters, the four simulations produce convective cloud elements that have essentially the same vertical characteristics.

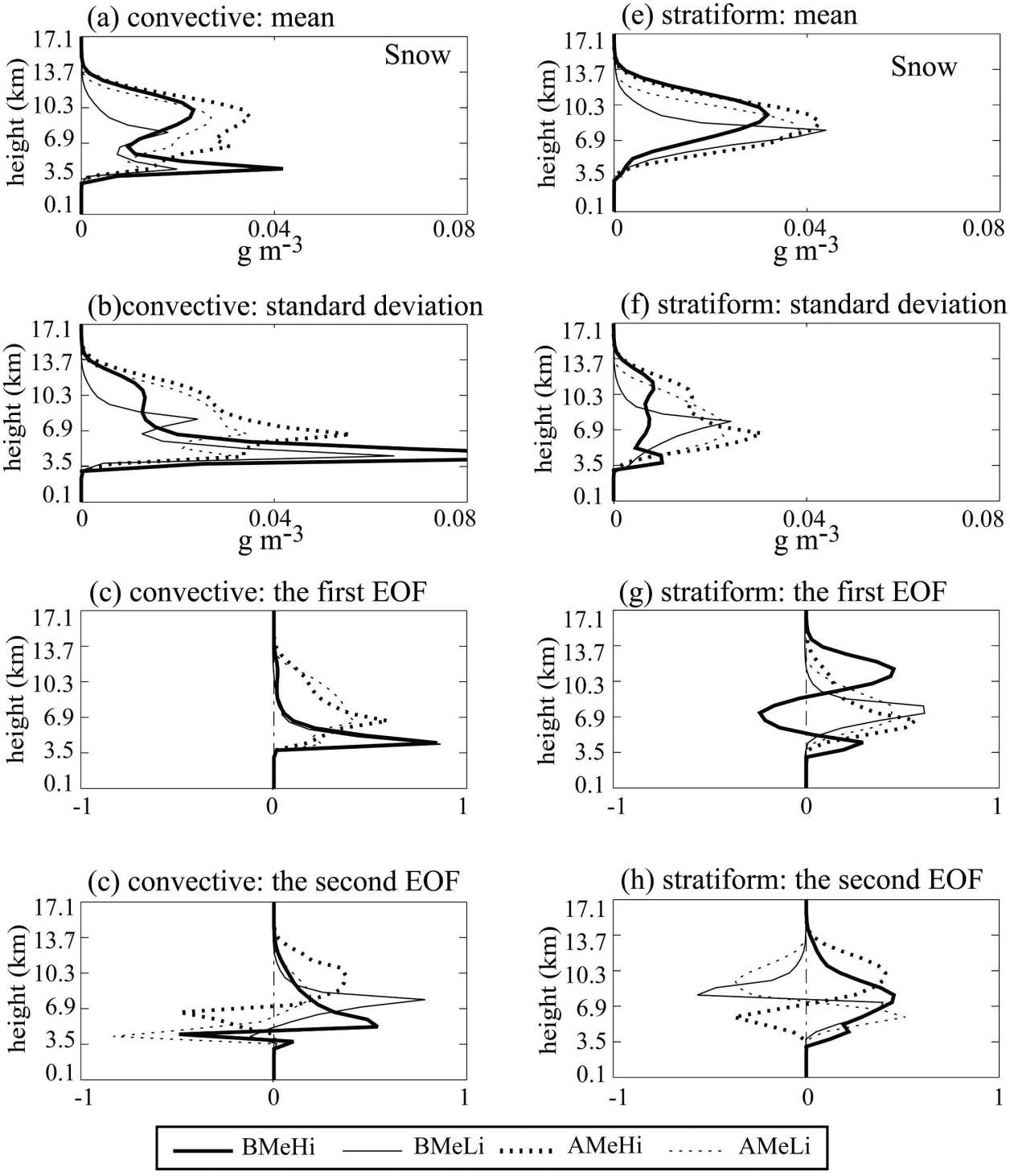

FIG. 6. Vertical profiles of the (from top row to bottom row) mean, the standard deviation, and the two dominant EOFs of snow in the (a)–(d) convective region and (e)–(h) stratiform region. Solid (dashed) lines are for the scheme-B (scheme A) simulations, with thick (thin) patterns denoting runs with high (low) ice.

TABLE 2. The first and second eigenvalues of model variables in convective and stratiform clouds for the four simulations. All numbers represent percentages of the total variance. Regular and italic fonts represent the first and second eigenvalues, respectively.

	BM_eH_i				AM_eH_i				BM_eL_i				AM_eL_i			
Variables	Convective		Stratiform		Convective		Stratiform		Convective		Stratiform		Convective		Stratiform	
Water vapor	76	*10*	81	*9*	72	*12*	78	*11*	76	*21*	79	*9*	70	*21*	75	*13*
Cloud water	70	*21*	50	*27*	69	*22*	48	*30*	63	*24*	60	*19*	65	*23*	55	*17*
Rain	90	*9*	90	*8*	89	*9*	93	*6*	90	*9*	88	*11*	88	*9*	92	*7*
Cloud ice	74	*16*	67	*16*	76	*14*	64	*24*	90	*6*	80	*9*	84	*10*	78	*11*
Snow	86	*5*	30	*26*	70	*14*	62	*20*	80	*15*	77	*14*	65	*19*	60	*27*
Graupel	86	*11*	89	*8*	87	*9*	92	*6*	90	*7*	87	*10*	88	*7*	89	*9*
Radar reflectivity	71	*23*	96	*3*	92	*3*	98	*1*	93	*2*	93	*5*	92	*3*	98	*1*
Vertical motion	72	*15*	37	*18*	66	*19*	35	*19*	59	*25*	32	*23*	64	*22*	31	*20*
Latent heating	78	*16*	73	*13*	74	*19*	75	*17*	65	*26*	67	*22*	71	*22*	72	*21*

In the stratiform region (Figs. 5c,d), there are slight differences in the magnitudes of the mean and standard deviations of vertical velocity and latent heating among the four simulations. However, the dominant variability in vertical structure is essentially identical as indicated by the overlapping curves for the first EOF. Systematic differences between scheme A and B do show up in the second EOF for vertical motion and latent heating in the high-ice simulations. Experiment BM_eH_i produced more complex perturbations for both quantities. For vertical motion in the stratiform region, BM_eH_i yielded perturbations of the same sign in two layers, one at lower levels (centered at 3.5-km altitude) and one at upper levels (centered at 12-km altitude), with perturbations of the opposite sign at midlevels (centered at 7 km). The other three simulations had less complex variability with perturbations of the opposite sign at low levels and upper levels. These perturbations are associated with variation in the strength of the mesoscale updraft aloft and mesoscale downdraft beneath.

The more complex pattern of variability in BM_eH_i is consistent with the type of deep subsidence that was found in the transition zone—the area adjacent to and to the rear of the convective line—of a similar midlatitude squall line observed by Biggerstaff and Houze (1993). They found an upper-level downdraft associated with compensating subsidence around the convective region and a low-level downdraft associated with evaporative cooling in the transition zone. In the BM_eH_i simulation, this pattern of variability is also associated with a more complex pattern in the variability of latent heating, as was hypothesized by Biggerstaff and Listemaa (2000). Furthermore, Biggerstaff and Houze (1993) showed that the transition zone had higher reflectivity aloft and lower reflectivity near the surface than did the remainder of the stratiform region. The BM_eH_i simulation shows a similar pattern of variability in the first EOF of the snow profile (Fig. 6g), in which perturbations of the opposite sign are found at mid- and upper levels. In contrast, the other simulations exhibit a single peak in the perturbations of the first EOF for snow at midlevels.

As noted in the discussion of the mean profiles, the simulations with scheme B exhibit greater sensitivity to the assumed concentration of activated ice crystals at 0°C than do the simulations based on scheme A. In the case in which significant amounts of cloud ice are generated, scheme B exhibited signs of a developing transition zone. For the limited number of experiments conducted here, the implementation of microphysical parameterizations in scheme A did not generate a similar transition zone feature.

b. Similarities and differences in eigenvalues from the four simulations

Eigenvalues from the EOF analysis (Table 2) quantify the amount of the total variation explained by the corresponding EOF. Overall, eigenvalues of the first and second EOFs for hydrometeor species of the four microphysical schemes explain about 70%–90% and 10%–20%, respectively, of their total variances in both convective and stratiform clouds. In particular, rainwater, graupel, and reflectivity all have high eigenvalues for the first EOF in each simulation. Hence, the vertical structure of the variability in hydrometeor profiles is relatively simple, with only one or two major modes. Except for stratiform-region cloud water, for which the first EOF only explains about 50%–60% of the total variation, an individual hydrometeor profile could be fairly well approximated by the mean profile plus the first EOF. Even for stratiform-region cloud water, a fairly accurate reconstruction would require only the first two EOFs.

In contrast, the vertical velocity profiles, especially in stratiform regions, led to the smallest eigenvalues in each simulation. The increased complexity of the vertical velocity structure in stratiform clouds seems contradictory to the conceptual models of stratiform re-

gions (e.g., Houze 1989) in which there is a broad and uniform mesoscale updraft above a uniform mesoscale downdraft. The dissipating convective cells that produce the stratiform region in the simulations apparently still contain residual convective-scale vertical drafts that lead to the complex variability of vertical motion in this area. This type of structure is consistent with vertical motions derived from dual-Doppler analyses of midlatitude squall lines (e.g., Biggerstaff and Houze 1993).

In terms of the eigenvalues for the first two EOFs, the four simulations had nearly identical results. The lone exception was for the first eigenvalue of snow in which the BM_eH_i simulation had notably less variance explained by the first EOF than did the other simulations. This result is consistent with the area classified as stratiform in the BM_eH_i simulation containing elements that are more typical of the structure of a transition zone (Biggerstaff and Houze 1993) than do the other three simulations.

c. *Utility of the EOF analysis for model comparisons*

Had the comparisons of the simulations relied on descriptive qualities of the storm systems, the BM_eL_i run might have been deemed the outlier because of the compact size of the simulated storm. With the EOF analysis, however, we see that BM_eL_i has very similar convective and stratiform elements to the two scheme-A runs. It is the stratiform rain region in the high-ice version of scheme B that is most unlike the other simulations.

The EOF analysis also provides insight to the importance of different physical processes parameterized in the two microphysical schemes. For example, the mean profile of snow over the convective region (Fig. 3d) shows a distinct double peak in snow concentration for scheme B as opposed to the single peak, or very weak double peak, in scheme A. The dominant variability pattern represented by the first EOF shows that the variability in the concentration of snow in the convective region in scheme B is confined to a narrow layer just above the freezing level (Fig. 6c). In contrast, for scheme A, the variability is spread over a deeper layer. This difference is attributed to the faster production of snow in scheme A in which the amount of cloud ice produced is less sensitive to the input microphysical parameters and the conversion of cloud ice to snow is less dependent on the presence of supercooled cloud water than in scheme B. This condition leads to higher concentrations of snow in scheme A that, when scavenged by graupel at lower altitudes, produce a quasi-monotonically decreasing snow profile. In other words, there is still plenty of snow left over after collection by graupel has occurred.

In scheme B, the production of snow occurs at a slower rate because the cloud-ice production is sensitive to the NCIO parameter and the conversion of cloud ice to snow through the Bergeron process requires supercooled cloud water. This situation limits the accumulation of snow in scheme B and, when scavenged by graupel at lower altitudes, rapidly depletes the snow content in those convective elements containing graupel. Convective elements with little graupel retain their snow accumulations, leading to the apparent double peak in snow concentrations in the mean profile. Hence, with the aid of the vertical variability patterns generated by the EOF analysis, it is easier to diagnose the physical processes contributing to the observed differences in the simulated storms.

6. Relationship between hydrometeors and T_B

a. *Sensitivity of T_B to hydrometeor species*

Before relating the mean hydrometeor structure to model-derived T_B, it is useful to illustrate the impact of a specific hydrometeor species to the upwelling radiances at 10 and 85 GHz, which are the two most independent frequencies examined here (Wilheit 1986). The sensitivity was determined by computing the 10- and 85-GHz T_B with all but one hydrometeor species present and comparing those with a control run that used all of the hydrometeor species. It is important to note that the hydrometeor species was removed only in the radiative transfer calculations and not in the actual simulations. This exercise provides a quantitative scale showing the impact of each hydrometeor species on the model-derived T_B at these two frequencies. This can be used to compare the current model results with other sets of simulations. For brevity, only the results from the AM_eL_i and AM_eH_i simulations are presented, because the calculations did not prove to be sensitive to the type of scheme used.

1) IMPACT ON 10-GHZ T_B

The calculations with no rain had a significant impact in the determination of T_B at 10 GHz over ocean in both convective and stratiform clouds for all four microphysical schemes. In convective areas (Figs. 7a,b), the rainwater contributed up to 150 K to the T_B at 10 GHz. A contribution of about 10 K to 10-GHz T_B by cloud water was evident at low T_B where the amount of rainwater present had not yet saturated the calculation (cf. Fig. 1). The low-ice run AM_eL_i shows that cloud water was able to contribute up to 25 K at the extreme

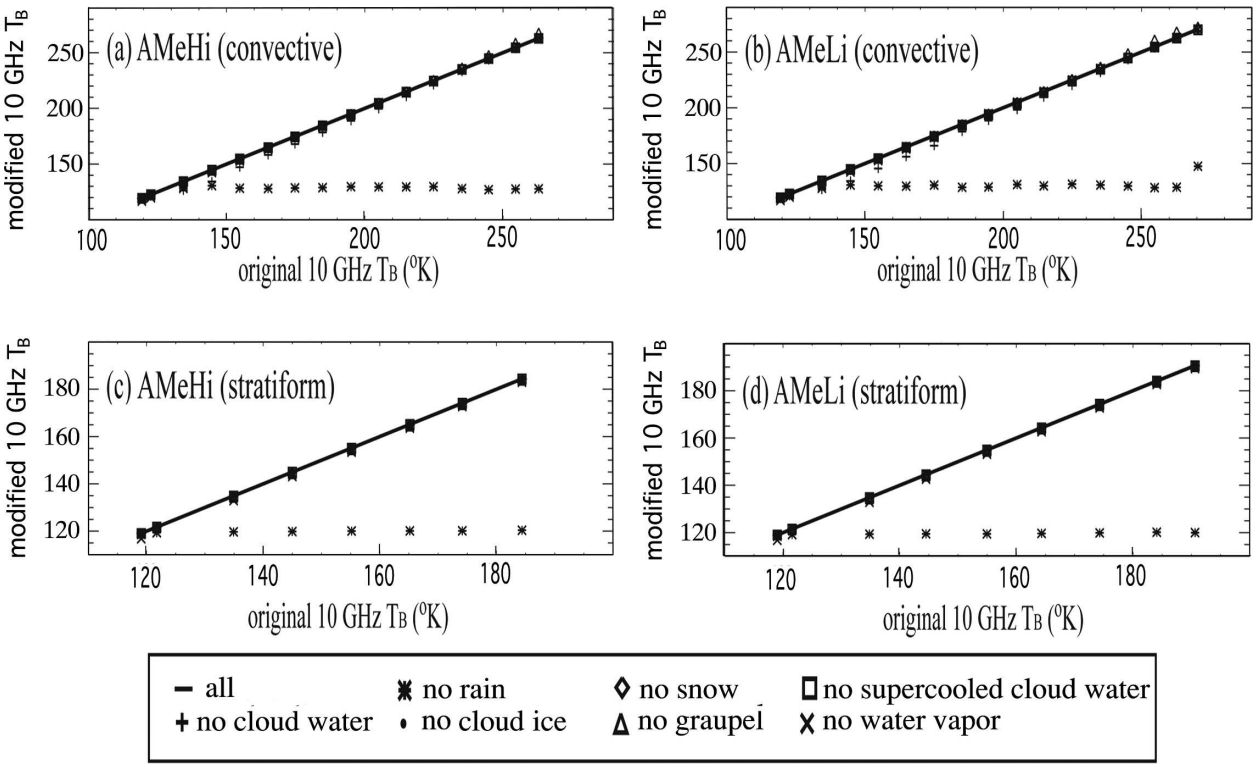

FIG. 7. Impact of individual hydrometeor species on 10-GHz T_B for (a) AM_eH_i and (b) AM_eL_i convective regions and (c) AM_eH_i and (d) AM_eL_i stratiform regions. The black solid lines are the control run using all hydrometeor species. The other symbols represent the calculations without the indicated hydrometeor species.

end of the convective distribution when rainwater was eliminated from consideration. This result explains the jump in modified T_B evident in the no-rain distribution between 260 and 270 K in AM_eL_i. Warming by cloud water was less evident in the high-ice simulation. For stratiform clouds, the warming by rain approached 70 K at the extreme end of the distribution. The accumulation of cloud water in the stratiform region was too low to increase the 10-GHz T_B by any noticeable degree.

Calculations without graupel showed that even at 10 GHz the graupel in the model scattered enough energy to lower the T_B by a few degrees at the extreme warm end of the T_B distribution. Thus, profiles with heavy rain were also associated with deep layers of significant graupel. Other hydrometeor species such as water vapor, cloud ice, and snow had little impact on 10-GHz T_B in the presence of rainwater.

2) IMPACT ON 85-GHZ T_B

At 85 GHz, the calculations with no graupel had the most impact on the resulting T_B (Fig. 8). For the simulations conducted here, 85-GHz T_B depressions extended up to about 170 K in the convective region because of the existence of high concentrations of graupel. Extremely low 85-GHz T_B (~100 K) have been observed over ocean by TRMM (Toracinta et al. 2002). Given the 2×2 km^2 scale of the model computational grid, the large depressions found in the intense convective cores of the simulations are within reason. On the other hand, depressions as high as 100 K in 85-GHz T_B were also evident in the simulated stratiform rain regions. This is a result of the inherent limitation of bulk three-class ice microphysical parameterizations in which stratiform rain mainly comes from melting high-density graupel that falls faster than the low-density snow. In nature, stratiform rain is generally associated with the melting of lower-density particles (Houghton 1968) that do not scatter as much 85-GHz radiation as do the higher-density graupel. As a consequence, the retrieval of stratiform rain based on passive microwave T_B–rain rate relations derived from cloud models is likely to produce significant uncertainty unless the higher-frequency channels are given low weight.

The other hydrometeor species that had an appreciable impact on 85-GHz T_B were water vapor and cloud water. Water vapor contributed about 45 K to the 85-GHz T_B in both convective and stratiform clouds in the T_B range of about 230–250 K. At colder tempera-

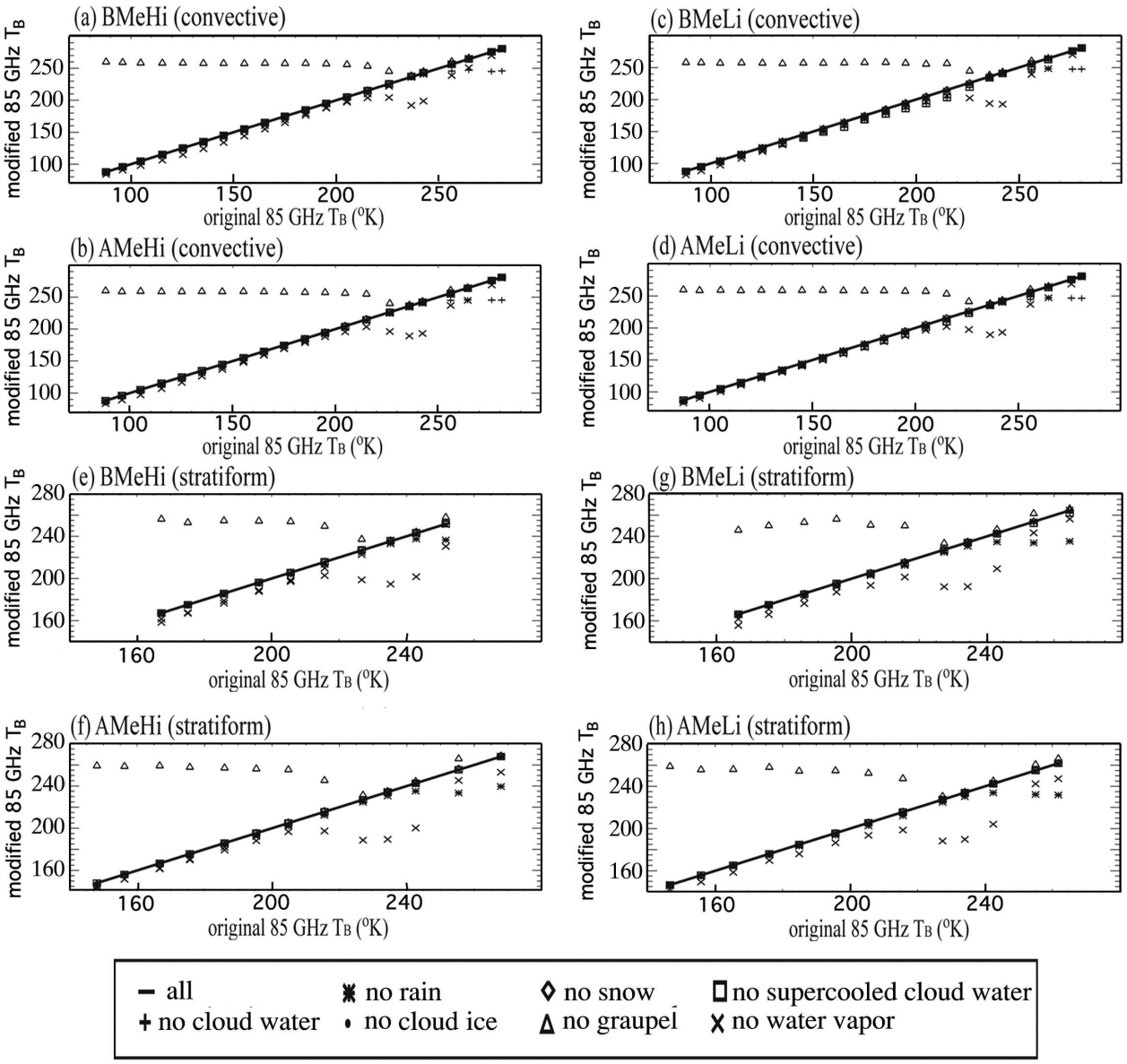

FIG. 8. Impact of individual hydrometeor species on 85-GHz T_B for (a) BM_eH_i, (b) AM_eH_i, (c) BM_eL_i, and (d) AM_eL_i convective regions and (e) BM_eH_i, (f) AM_eH_i, (g) BM_eL_i, and (h) AM_eL_i stratiform regions. The black solid lines are the control run using all hydrometeor species. The other symbols represent the calculations without the indicated hydrometeor species.

tures, the impact of water vapor was masked by the decrease in T_B associated with graupel. Because the bulk of the water vapor mass is in the lowest part of the atmosphere, any upwelling emission would be effectively scattered away by the thick graupel layer above.

Calculations separating the effect of all cloud water from just supercooled cloud water showed that it was the supercooled cloud water that affected the 85-GHz T_B in the presence of graupel. In the low-ice run, supercooled cloud water warmed the 85-GHz T_B by an average of about 15 K over the convective region (Figs. 8c,d). Maximum warming in individual profiles was close to the 80 K reported by Adler et al. (1991) in their simulations. More important, however, the calculations here indicate that the warming of 85-GHz T_B by supercooled cloud water is unimportant when large concentrations of graupel are present. Even with abundant supercooled cloud water, the scattering effect by graupel appears to be dominant at 85-GHz T_B of less than about 150 K (Fig. 8c).

Note also that the amount of supercooled cloud water produced in the simulations is dependent on the

specific model microphysical parameterization used. The high-ice runs had little supercooled water in either scheme whereas the low-ice runs had appreciable amounts. Thus, the effect of supercooled cloud water, even in scheme A, can be exaggerated or understated depending on the choice of NCIO. Given the magnitude of its impact on 85-GHz T_B, proper parameterization of supercooled cloud water may be crucial to retrieving rainfall and latent heating profiles correctly from passive microwave observations.

In general, T_B at TMI channels over water seem to be little affected by cloud ice and snow. More sophisticated calculations for snow, such as the discrete dipole approximation (Draine and Flatau 1994), tend to yield cooler 85-GHz T_B than the Mie approximation (Liu 2004), but the differences are only a few degrees at most. In the presence of high graupel concentrations, the additional cooling would be insignificant. Part II shows that the lack of sensitivity to cloud ice and snow leads to poor performance in the retrieval of EOF coefficients associated with latent heating in stratiform rain regions. Unfortunately, the greatest difference between scheme-A and scheme-B microphysical parameterizations is in the cloud ice and snow profiles. Quantitative evaluation of cloud model performance for a particular case could be performed if high-resolution observations of passive microwave signatures over an appropriate oceanic storm system were collected and included additional frequencies sensitive to cloud ice and, if possible, snow.

b. Correlation between cloud properties and TMI T_B

In this section, the EOF analysis method is used in conjunction with calculated brightness temperatures to quantify the relationship between cloud properties and individual T_B at TMI frequencies. The first EOF coefficients of the model variables were sorted according to the brightness temperatures, and correlations between the EOF coefficients and TMI T_B were determined. The correlations of the first EOF coefficient for each model variable against each TMI frequency for all four simulations are given in Table 3.

1) SIMILARITIES AMONG THE SIMULATIONS

Most of the correlations are generally similar among all four simulations. Profiles of rain, graupel, and radar reflectivity were well correlated with at least one of the TMI frequencies in both convective and stratiform regions and show little variation within the different microphysical parameterizations. In general, these parameters were strongly positively correlated with 10-GHz T_B and strongly negatively correlated with 85-GHz T_B. Little variation among the simulations was also found for water vapor, vertical motion, and latent heating. These fields were generally poorly correlated with the TMI T_B, especially over the stratiform rain regions, however. Convective-region vertical velocity and latent heating showed moderately high correlation only at 10 GHz and showed even lower anticorrelation at 85 GHz. The decreased skill at 85 GHz is unfortunate because that channel is able to provide information over land whereas the 10-GHz channel is only useful over surfaces with low emissivity, like the ocean. Hence, retrievals of latent heating based on 85-GHz T_B are likely to be less certain than retrievals based on 10-GHz T_B.

The correlation between surface rain rate and TMI T_B is high at 10 GHz, but not as high as the correlation between the first EOF of the rain profile and 10-GHz T_B. The strong anticorrelation with 85 GHz was also weaker for the surface rain rate, especially for the stratiform region of the BM_eL_i simulation.

2) DIFFERENCES AMONG THE SIMULATIONS

The correlations between cloud ice, cloud water, and snow with TMI T_B depended on the particular microphysical scheme or the value chosen for the initial concentration of activated ice crystals at 0°C. As might be expected, stratiform region cloud water was correlated with T_B only in the simulations that had limited production of cloud ice so that cloud water could accumulate—that is, the AM_eL_i and BM_eL_i low-NCIO runs. Otherwise, the lack of appreciable cloud water concentrations resulted in correlations of near zero at all TMI frequencies.

The remaining differences among the simulations show the inherent difference in the behavior of the microphysical parameterization schemes. It was found that cloud ice was actually well positively (negatively) correlated with 10-GHz (85-GHz) T_B in the AM_eH_i simulation despite cloud ice having little affect on the calculation of brightness temperatures. This result is a consequence of the A-type scheme concentrating large quantities of cloud ice in regions of high graupel content. In contrast, the B-type scheme contains large concentrations of cloud ice everywhere. Indeed, the BM_eL_i simulation had the weakest correlation between cloud ice and TMI T_B because the total content of cloud ice was lower than in the corresponding B-scheme high-ice run and what ice was present was more uniformly distributed than in the corresponding A-scheme low-ice run. A similar dichotomy was found for snow. The A-type simulations exhibited fairly strong anticorrelation with 85-GHz T_B, but the B-type simulations did not. This difference was partially related to the lack of significant snow accumulation in the B-type simulations

TABLE 3. Correlation between T_B at each TMI frequency and the first EOF coefficients of each model variable. There are four rows for each variable. Each row represents a microphysical scheme in the order of BM_eH_i, AM_eH_i, BM_eL_i, and AM_eL_i. Regular and italic fonts represent convective and stratiform clouds, respectively.

Correlation	10 GHz		19 GHz		21 GHz		37 GHz		85 GHz	
Water vapor	−0.24	*−0.10*	−0.23	*−0.04*	−0.18	*0.03*	−0.02	*−0.10*	0.41	*0.38*
	−0.29	*−0.14*	−0.29	*−0.12*	−0.23	*−0.08*	−0.01	*−0.17*	0.48	*0.41*
	−0.31	*−0.08*	−0.29	*−0.07*	−0.22	*−0.04*	−0.02	*−0.12*	0.46	*0.25*
	−0.31	*−0.05*	−0.31	*−0.03*	−0.25	*0.01*	−0.03	*−0.08*	0.47	*0.28*
Cloud water	0.19	*−0.03*	0.32	*−0.01*	0.40	*0.01*	0.59	*−0.01*	0.33	*0.11*
	0.13	*−0.02*	0.27	*−0.01*	0.36	*0.00*	0.57	*−0.02*	0.39	*0.10*
	0.17	*0.30*	0.35	*0.32*	0.44	*0.32*	0.61	*0.34*	0.44	*−0.22*
	0.12	*0.32*	0.28	*0.34*	0.36	*0.34*	0.56	*0.35*	0.44	*−0.29*
Rain	0.96	*0.90*	0.84	*0.90*	0.73	*0.88*	0.27	*0.86*	−0.70	*−0.66*
	0.96	*0.91*	0.78	*0.91*	0.63	*0.90*	0.10	*0.87*	−0.75	*−0.75*
	0.94	*0.92*	0.71	*0.92*	0.53	*0.92*	0.05	*0.88*	−0.68	*−0.43*
	0.94	*0.91*	0.71	*0.91*	0.52	*0.90*	0.01	*0.86*	−0.72	*−0.64*
Cloud ice	0.64	*0.30*	0.56	*0.28*	0.46	*0.24*	0.08	*0.34*	−0.76	*−0.42*
	0.73	*0.65*	0.54	*0.67*	0.39	*0.66*	−0.09	*0.66*	−0.74	*−0.75*
	0.40	*0.13*	0.40	*0.12*	0.34	*0.11*	0.13	*0.15*	−0.43	*−0.19*
	0.66	*0.44*	0.40	*0.46*	0.20	*0.46*	−0.27	*0.45*	−0.78	*−0.59*
Snow	0.68	*0.34*	0.56	*0.37*	0.49	*0.36*	0.21	*0.42*	−0.39	*−0.37*
	0.69	*0.48*	0.62	*0.49*	0.51	*0.48*	0.09	*0.51*	−0.72	*−0.58*
	0.59	*0.08*	0.41	*0.08*	0.31	*0.07*	0.07	*0.12*	−0.26	*−0.12*
	0.69	*0.33*	0.58	*0.34*	0.44	*0.34*	0.01	*0.37*	−0.73	*−0.41*
Graupel	0.73	*0.70*	0.58	*0.71*	0.44	*0.68*	−0.08	*0.70*	−0.90	*−0.85*
	0.77	*0.80*	0.54	*0.81*	0.36	*0.80*	−0.21	*0.78*	−0.88	*−0.89*
	0.73	*0.67*	0.41	*0.69*	0.18	*0.69*	−0.31	*0.67*	−0.84	*−0.77*
	0.75	*0.76*	0.43	*0.78*	0.19	*0.77*	−0.33	*0.74*	−0.85	*−0.85*
Radar reflectivity	0.61	*0.77*	0.46	*0.76*	0.34	*0.74*	−0.06	*0.69*	−0.59	*−0.65*
	0.61	*0.89*	0.40	*0.87*	0.25	*0.84*	−0.17	*0.78*	−0.59	*−0.83*
	0.60	*0.72*	0.29	*0.73*	0.10	*0.71*	−0.29	*0.66*	−0.63	*−0.59*
	0.57	*0.86*	0.30	*0.84*	0.12	*0.82*	−0.27	*0.75*	−0.59	*−0.76*
Vertical motion	0.57	*0.35*	0.40	*0.37*	0.32	*0.37*	0.02	*0.38*	−0.44	*−0.31*
	0.60	*0.37*	0.39	*0.37*	0.27	*0.37*	−0.08	*0.35*	−0.46	*−0.37*
	0.64	*0.40*	0.37	*0.41*	0.21	*0.41*	−0.12	*0.41*	−0.45	*−0.34*
	0.62	*0.30*	0.35	*0.31*	0.18	*0.31*	−0.16	*0.30*	−0.48	*−0.29*
Latent heating	0.60	*0.18*	0.42	*0.19*	0.32	*0.19*	−0.01	*0.19*	−0.49	*−0.14*
	0.60	*0.10*	0.38	*0.10*	0.25	*0.10*	−0.12	*0.09*	−0.49	*−0.09*
	0.61	*0.07*	0.35	*0.07*	0.19	*0.07*	−0.13	*0.07*	−0.44	*−0.07*
	0.60	*0.04*	0.32	*0.04*	0.15	*0.04*	−0.19	*0.03*	−0.47	*−0.05*
Precipitation at surface	0.87	*0.86*	0.76	*0.85*	0.67	*0.83*	0.25	*0.78*	−0.64	*−0.55*
	0.85	*0.88*	0.70	*0.87*	0.57	*0.86*	0.09	*0.80*	−0.69	*−0.65*
	0.84	*0.83*	0.63	*0.82*	0.47	*0.82*	0.03	*0.77*	−0.64	*−0.32*
	0.83	*0.87*	0.62	*0.86*	0.46	*0.85*	−0.00	*0.79*	−0.67	*−0.56*

and partially related to the snow being more uniformly distributed. Because snow accounted for almost 30% of the surface rain in the stratiform region (Fig. 3), the variability in the correlations between snow and 85-GHz T_B also contributed to variability in correlations between surface rain rate and 85-GHz T_B in stratiform regions. Snow contributed very little to surface rain rate over convective areas. Hence, the correlations between 85-GHz T_B and surface rain rate were unaffected by the influence of snow over convective regions.

The variability in the correlations between the first EOF coefficients and TMI T_B for cloud ice, cloud water, and snow strongly suggests that the model microphysics can have a significant impact on the relationships between hydrometeor profiles and derived brightness temperatures at TMI frequencies. This suggestion is examined further in Part II, which uses the correlations presented here as weighting factors in determining the structural differences in hydrometeor profiles associated with small changes in the input brightness temperatures at the TMI frequencies.

3) IMPACT OF SCALE

The correlations in Table 3 are based on analysis at a scale comparable to the scale of individual convective elements. This approach facilitates interpretation of the

TABLE 4. Correlations between T_B at 10 and 85 GHz and the first EOF coefficient of each model variable at three different resolutions (i.e., pixels). Only pixels in which more than 75% of the individual profiles were convective were used. There are four rows for each variable. Each row represents a microphysical scheme in the order of BM_eH_i, AM_eH_i, BM_eL_i, and AM_eL_i.

Correlation	10 GHz, 6×6 km^2	10 GHz, 36×36 km^2	10 GHz, 72×72 km^2	85 GHz, 6×6 km^2	85 GHz, 36×36 km^2	85 GHz, 72×72 km^2
Water vapor	−0.24	−0.27	−0.23	0.41	0.30	0.28
	−0.29	−0.26	−0.24	0.48	0.34	0.36
	−0.31	−0.28	−0.16	0.46	0.46	0.34
	−0.31	−0.24	−0.07	0.47	0.45	0.30
Cloud water	0.19	0.03	0.09	0.33	0.24	0.22
	0.13	0.09	0.18	0.39	0.25	0.21
	0.17	0.11	0.14	0.44	0.42	0.39
	0.12	0.13	0.17	0.44	0.42	0.35
Rainwater	0.96	0.63	0.62	−0.70	−0.42	−0.45
	0.96	0.65	0.66	−0.75	−0.40	−0.43
	0.94	0.94	0.93	−0.68	−0.70	−0.69
	0.94	0.93	0.93	−0.72	−0.69	−0.64
Cloud ice	0.64	0.44	0.45	−0.76	−0.45	−0.44
	0.73	0.43	0.44	−0.74	−0.45	−0.50
	0.40	0.62	0.59	−0.43	−0.78	−0.77
	0.66	0.36	0.22	−0.78	−0.49	−0.35
Snow	0.68	0.43	0.43	−0.39	−0.42	−0.39
	0.69	0.46	0.50	−0.72	−0.20	−0.23
	0.59	0.69	0.66	−0.26	−0.70	−0.64
	0.69	0.58	0.51	−0.73	−0.18	−0.04
Graupel	0.73	0.47	0.47	−0.90	−0.53	−0.56
	0.77	0.48	0.44	−0.88	−0.52	−0.59
	0.73	0.71	0.71	−0.84	−0.86	−0.85
	0.75	0.71	0.69	−0.85	−0.84	−0.86
Radar reflectivity	0.61	0.37	0.36	−0.59	−0.32	−0.35
	0.61	0.39	0.35	−0.59	−0.31	−0.34
	0.60	0.55	0.56	−0.63	−0.59	−0.61
	0.57	0.56	0.56	−0.59	−0.64	−0.65
Vertical motion	0.57	0.40	0.40	−0.44	−0.28	−0.28
	0.60	0.36	0.39	−0.46	−0.24	−0.27
	0.64	0.60	0.64	−0.45	−0.45	−0.43
	0.62	0.62	0.56	−0.48	−0.41	−0.36
Latent heating	0.60	0.39	0.41	−0.49	−0.31	−0.31
	0.60	0.40	0.46	−0.49	−0.28	−0.31
	0.61	0.62	0.64	−0.44	−0.47	−0.45
	0.60	0.64	0.61	−0.47	−0.44	−0.36
Surface rain rate	0.87	0.71	0.70	−0.64	−0.24	−0.20
	0.85	0.71	0.73	−0.69	−0.23	−0.21
	0.84	0.78	0.74	−0.64	−0.63	−0.64
	0.83	0.79	0.78	−0.67	−0.65	−0.57

differences among the simulations to parameterizations of physical processes that are incorporated in the cloud model. Direct application to satellite-based retrievals is complicated by the statistical effects of averaging over the satellite footprint's field of view, which may contain numerous cloud elements at various stages of evolution, and the particular geometry of the satellite's instrument and its orbit. To determine how significant the impact of microphysical parameterizations is at scales that are more consistent with actual satellite footprint sizes, the correlations have been recomputed for 36×36 km^2 and 72×72 km^2 footprints.

It is important to realize that the brightness temperature calculation is conducted at finescale and then averaged. This approach more closely resembles how an antenna collects information from a continuous cloud field than does using a mean cloud profile to calculate a mean brightness temperature. Because cloud property– T_B relations have been shown to depend on cloud type (Olson et al. 1999), we made use of only the footprints in which more than 75% of the individual profiles contained the same classification. Only the correlations over convective regions at 10 and 85 GHz are shown (Table 4) because the limited extent of the stratiform

precipitation region leads to too few stratiform footprints for meaningful correlations at these large scales.

In general, the correlations that were relatively high at finescale tended to become weaker as the size of the satellite footprint increases. This result should be expected. There is a nonlinear relationship between cloud hydrometeors and brightness temperature. As different cloud profiles get averaged together, the correlation between the mean cloud structure and the averaged brightness temperature should decrease. Perhaps surprising is that most of the decrease in correlation with increasing footprint occurs by 36×36 km^2. Not much additional loss was found at 72×72 km^2. Apparently the variability of the simulated convection was statistically robust by 36×36 km^2 for the storms modeled here.

Averaging over larger scales also diminished the distinction between the layered hydrometeor structure in scheme A and the more uniform hydrometeor distribution in scheme B for cloud ice and snow. At high resolution, scheme A exhibited a strong negative correlation between 85-GHz T_B and cloud ice and snow, despite the weak contribution those hydrometeors have on 85-GHz T_B, because of the tendency for high cloud-ice concentrations to coexist with high graupel concentrations. At coarser scales, the correlations are much lower for simulations using scheme A and are significantly higher for the BM_eL_i run. Because the relationship between cloud ice and graupel content varies during the evolution of a cloud element, the effect of averaging developing, mature, and dissipating convection diminished the tendency for high cloud-ice concentrations to coexist with high graupel concentrations. Hence, the statistical effects associated with satellite data resolution masked fundamental differences in the relationship between graupel and cloud-ice concentrations between schemes A and B that were evident at higher resolution.

In contrast, averaging accentuated a fundamental difference between the low-ice and high-ice simulations. For the high-ice runs, the correlations between 10- and 85-GHz T_B and many of the cloud properties (rainwater, graupel, radar reflectivity, vertical motion, and latent heating) decreased considerably at larger footprint sizes. For the low-ice runs, however, the correlations decreased only slightly as the footprint size increased. This difference is related to the greater range of convective cell structure produced in the low-ice runs, where both the mean value and the standard deviation of those cloud properties were greater.

One consequence of this behavior is that at coarse resolution the correlations between 10-GHz T_B and the first EOF of rainwater profile for the high-ice runs are lower than the correlations for surface rain rate. In physical terms, 10-GHz T_B should be better correlated with the integrated rain content as represented by the first EOF than with the rain rate at one level. In the low-ice simulations that physical relationship is retained. Hence, the impact of averaging over the scale of the satellite footprint depended on the microphysical parameter settings used in the cloud model.

c. *Profiles of hydrometeors sorted by T_B at 10 and 85 GHz*

To understand better the variability in microphysical and latent heating profiles associated with a given T_B for the four microphysical schemes, all vertical profiles have been classified in terms of 20-K increments in both 10- and 85-GHz T_B. Mean and EOFs of vertical profiles were computed for each increment in T_B.

1) SORTING BY 10 GHZ

Figure 9 shows the mean and first-EOF profiles obtained by sorting the convective-region vertical profiles by 10 GHz for the 240–260-K range, which represents the upper end of the observed 10-GHz T_B distribution, and sorting the stratiform-region profiles by 10 GHz for the range of 160–180 K, which represents the middle of the distribution. Both increments cover about 5% of the total number of profiles in the convective and stratiform databases. Given the high correlations between 10-GHz T_B and the first EOF coefficient of the rain profile, it should be expected that each simulation would have similar rain profiles for a fixed increment in 10-GHz T_B. This is indeed the case for both the convective and stratiform rain regions.

Comparison of the mean profiles of a cloud property with correlations between the first EOF coefficient of that cloud property and 10-GHz T_B (Table 3) shows that the variability of the mean profiles for a given cloud property generally increases with decreasing correlation. Once again, the variability in mean profiles of cloud ice, snow, and supercooled cloud water associated with fixed ranges of 10-GHz T_B indicates that these parameters are strongly dependent on the details of the cloud model microphysical parameterization schemes.

It is surprising that the mean profiles in vertical motion over the convective region are fairly similar despite having relatively low correlation with 10-GHz T_B. Only the BM_eH_i simulation stands out with stronger mean vertical motion and stronger net latent heating than the other three simulations. It is important to note that the profiles of vertical motion and latent heating are different even though the profiles of rain and radar reflectivity are virtually identical.

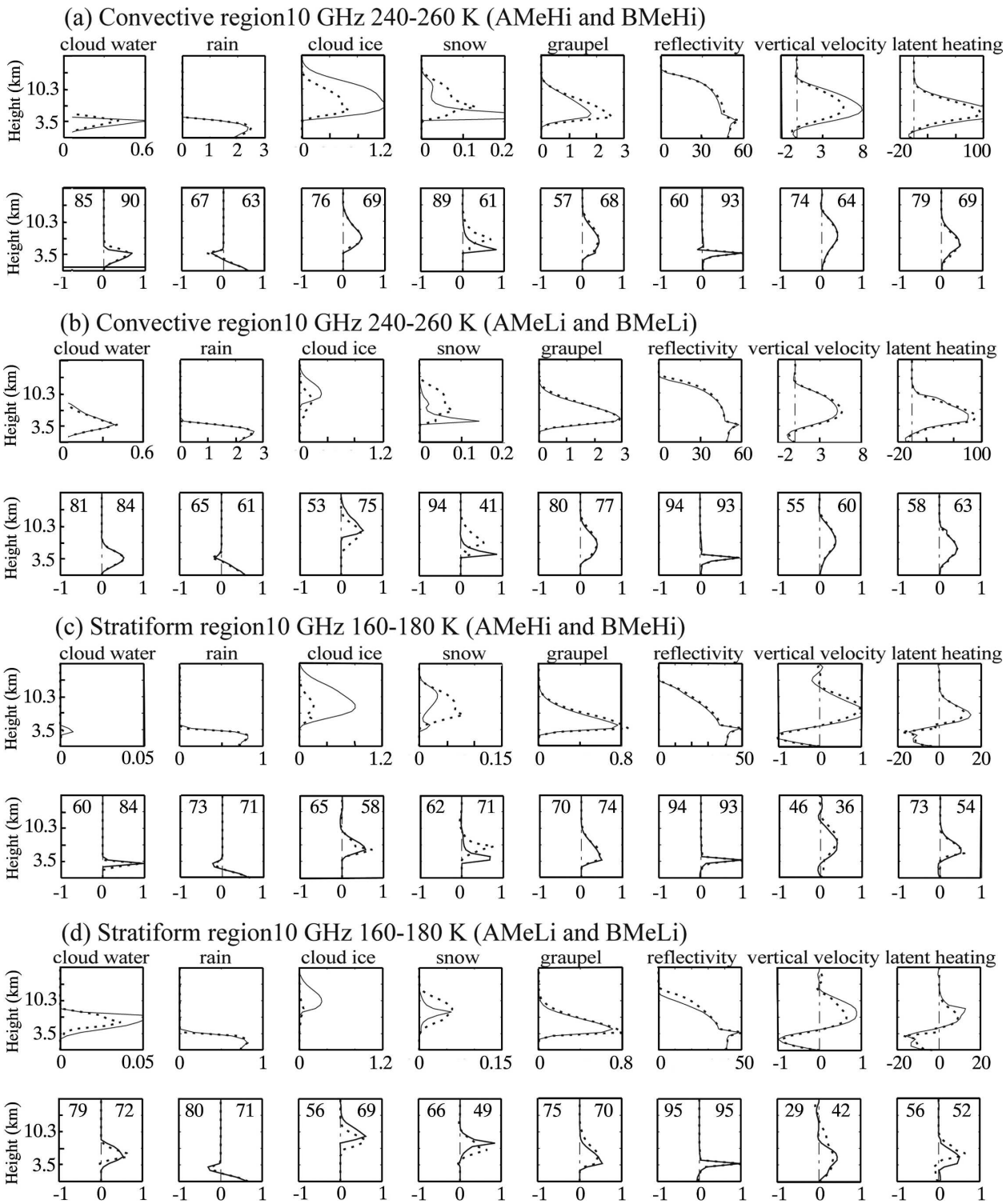

FIG. 9. Mean vertical profiles (the first row of each group) and the first EOFs (the second row) of hydrometeor species (g m^{-3}), radar reflectivity (dBZ), vertical velocity (m s^{-1}), and latent heat release (K h^{-1}) classified by 10 GHz for (a) the AM_cH_i and BM_cH_i convective regions, (b) the AM_cL_i and BM_cL_i convective regions, (c) the AM_cH_i and BM_cH_i stratiform regions, and (d) the AM_cL_i and BM_cL_i stratiform regions. Dotted (solid) lines denote scheme-A (scheme B) runs. The two numbers on the left and right sides in the EOF panels denote eigenvalues for scheme A and scheme B, respectively.

For the stratiform region, it is BM_eL_i that yields different mean profiles from the other three simulations. In that simulation, the concentration of cloud ice is shifted toward higher altitudes, with correspondingly higher altitude for the peak in mean vertical motion and net latent heating. Hartmann et al. (1984) and DeMaria (1985) showed that the atmosphere is sensitive to the vertical structure of the latent heating profile. The insensitivity of TMI frequencies to cloud ice and the importance of cloud ice to upper-level latent heating suggest that it may be difficult to retrieve latent heating accurately using TMI observations.

2) Sorting by 85 GHz

Classifying the vertical profiles by increments in 85-GHz T_B (Fig. 10) produced much the same variability as was found in the classification by 10-GHz T_B. The only difference is that the rain profiles exhibit a spread of about 15% in the amount of mean convective rain mass near the surface. Tao et al. (1993) suggested that a 10% difference in rain estimations across the Tropics would have a significant effect on the global latent heating by precipitation. As suggested by the analysis conducted here, relatively minor differences in the implementation of microphysical parameterizations can lead to variations in estimations of low-level rain mass of that magnitude.

7. Conclusions

The effect of model microphysics on the relationships between hydrometeor profiles, latent heating, and derived satellite microwave brightness temperatures was studied using a nonhydrostatic, adaptive-grid, three-dimensional cloud model initialized with an environment conducive to the formation of a leading-line trailing-stratiform squall line system. Two microphysical schemes (each employing a three-class ice bulk parameterization) were compared for both convective and stratiform precipitation using empirical orthogonal function analyses of the vertical profiles of hydrometeors, radar reflectivity, vertical velocity, and latent heating. Experiments were conducted for simulations that represented both environments in which supercooled cloud water is likely to accumulate and environments in which supercooled cloud water is typically not present in large quantities by adjusting NCIO, the number of ice crystals assumed to be activated at 0°C.

The type-A parameterization scheme, based on Tao and Simpson (1993), showed the least amount of sensitivity to changes in NCIO. The high-ice (high NCIO) and low-ice (low NCIO) simulations produced essentially the same size of storm system with essentially the same mean convective and stratiform region rainfall. The high-ice run did produce more snow and cloud ice than did the low-ice run. The EOF analysis indicated that the dominant anomaly pattern for cloud ice and snow was shifted to higher altitudes in the low-ice simulation. Yet, these changes were relatively minor in comparison with the sensitivity of the type-B scheme that was based on Keenan et al. (1994).

Hristova-Veleva (2000) noted that the parameterization of cloud ice was more dependent on NCIO in scheme B. Moreover, the conversion of cloud ice to snow through the Bergeron process was dependent on the presence of supercooled water in scheme B. These factors lead to a significant sensitivity in the size and vertical structure of the simulated storm for the two types of environments. When viewed in terms of the horizontal dimensions of the storm systems, the low-ice version of scheme B (BM_eL_i) would have been viewed as an outlier from the other simulations since it produced a much more compact storm system. However, the EOF analysis revealed that the vertical structure of the anomaly patterns for BM_eL_i was similar to that of the type-A simulations. Moreover, the EOF analysis showed that it was the high-ice version of scheme B, BM_eH_i, that had significantly different anomaly patterns for snow, vertical velocity, and latent heating in the stratiform region. The additional complexity evident in BM_eH_i is consistent with observations of vertical motion and radar reflectivity through a transition zone (Biggerstaff and Houze 1993) that are often found immediately to the rear of the convective region of mature-stage leading-line trailing-stratiform squall line systems. Thus, the EOF analysis helped to elucidate which of the simulations had fundamentally different characteristics from the others.

The first EOF coefficients of cloud properties were correlated against brightness temperatures at TMI frequencies. For the liquid and high-density ice precipitation categories, the correlations from the four simulations were very similar. In contrast, at high resolution, the correlations for snow and cloud ice were dependent on which parameterization scheme was used. Despite cloud ice and snow having little impact on calculations of 85-GHz T_B, the type-A parameterization showed a fairly high correlation between snow and 85-GHz T_B for both environments and between cloud ice and 85-GHz T_B for the high-ice simulation at high resolution. This result was attributed to the tendency for that scheme to have large quantities of snow and cloud ice in the same location that had large quantities of graupel. Scheme B tended to have more uniform distributions of cloud ice and snow.

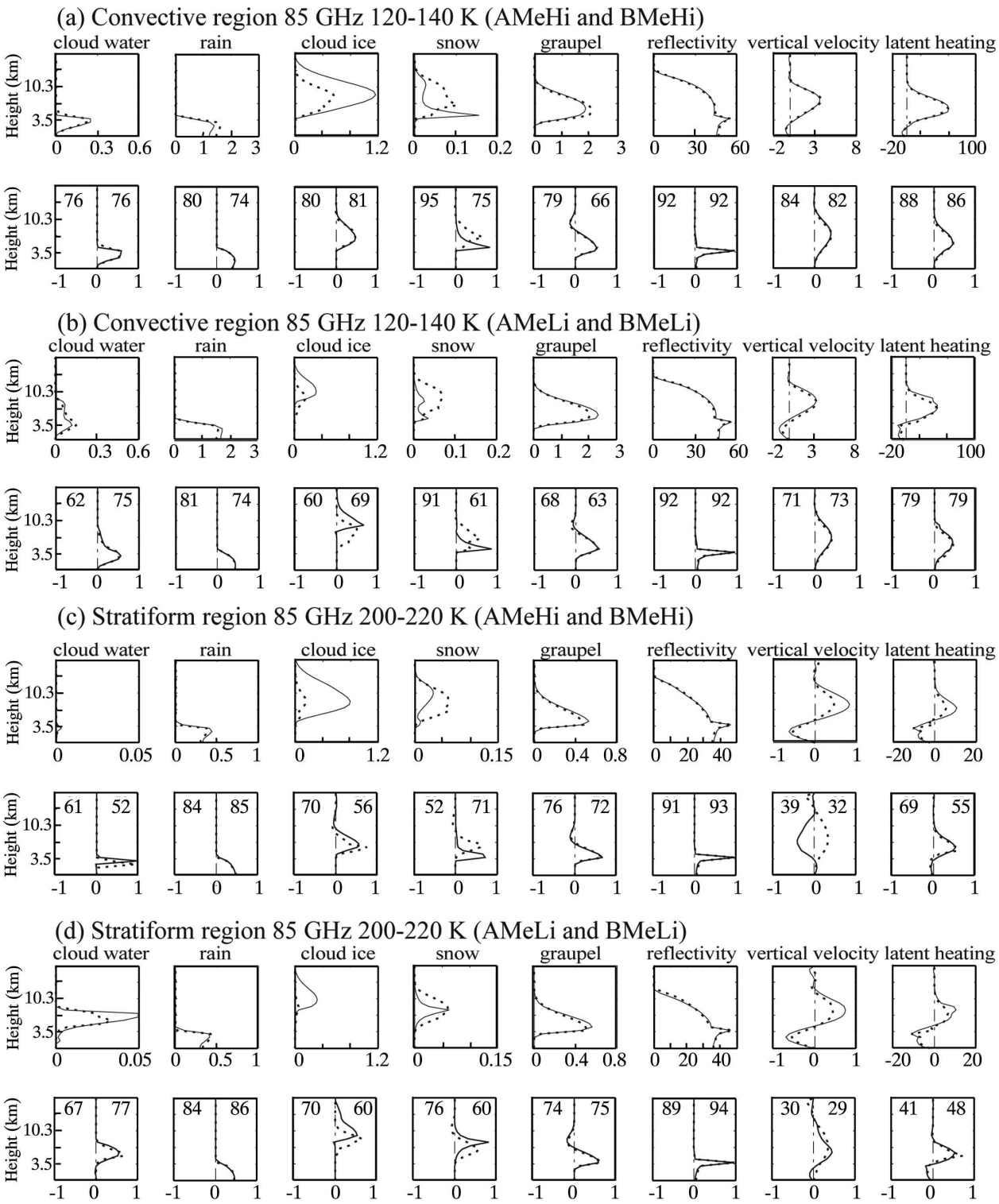

FIG. 10. Same as Fig. 9, but classified by 85 GHz.

At coarser resolutions, the ability to distinguish the effects of the layered hydrometeor structure in scheme A was diminished. Indeed, when the correlations were performed over 36×36 km^2 and 72×72 km^2 "footprints," the BM_eL_i simulation showed greater negative correlation between 85-GHz T_B and cloud ice and snow than did the simulations using scheme A. The change in behavior at different scales illustrates the importance of

using finescale analysis to evaluate physical uncertainty in retrievals of cloud properties.

Other effects of averaging over the scale of the satellite footprint depended on the microphysical parameter settings used in the cloud model. In the high-ice simulations, correlations between 10-GHz T_B and many of the cloud properties, including rainwater and latent heating profiles, decreased considerably at the coarser scales. In contrast, in the low-ice simulations, correlations between 10-GHz T_B and the same cloud properties decreased only slightly with increasing footprint size.

When the high-resolution vertical profiles of cloud properties were sorted by brightness temperatures, the impact of supercooled cloud water on 85-GHz T_B led to a variation of 15% in the mean convective rainfall at the surface from the four simulations. There were also significant differences in the mean profile of cloud ice, snow, and latent heating between the four simulations. The relative insensitivity of the TMI frequencies to cloud ice and snow and the importance of cloud ice to upper-level latent heating suggest that retrievals of these properties based on TMI observations are dependent on the particular details of the microphysical parameterizations used to construct the retrieval databases. In Part II it is found that this level of uncertainty was significant relative to the inherent nonuniqueness of hydrometeor profiles that can satisfy a given set of brightness temperatures.

Acknowledgments. This research was supported by the National Aeronautics and Space Administration (NASA) Tropical Rainfall Measuring Mission (TRMM) under Grants NAG 5-9697 and NAG 5-13262. The authors thank Dr. L. Wicker for his guidance in using the COMMAS model. We thank Drs. W.-K. Tao and B. Ferrier for providing their three-ice microphysical schemes and Dr. C. Kummerow for providing the radiative transfer model. Doctor W. Olson gave valuable advice in the beginning of this study, and Dr. T. Wilheit gave a helpful critique near the end of it.

REFERENCES

Adler, R. F., and A. J. Negri, 1988: A satellite infrared technique to estimate tropical convective and stratiform rainfall. *J. Appl. Meteor.,* **27,** 30–51.

——, H.-Y. M. Yeh, N. Pasad, W.-K. Tao, and J. Simpson, 1991: Microwave simulations of a tropical rainfall system with a three-dimensional cloud model. *J. Appl. Meteor.,* **30,** 924–953.

Austin, P. M., and A. C. Bemis, 1950: A quantitative study of the "bright band" in radar precipitation echoes. *J. Atmos. Sci.,* **7,** 145–151.

Battan, L. J., 1973: *Radar Observation of the Atmosphere.* University of Chicago Press, 324 pp.

Bergeron, T., 1935: On the physics of clouds and precipitation. *Proc. Fifth Assembly,* Vol. 2, Lisbon, Portugal, IUGG, 156–178.

Biggerstaff, M. I., and R. A. Houze Jr., 1991a: Kinematic and precipitation structure of the 10–11 June 1985 squall line. *Mon. Wea. Rev.,* **119,** 3034–3065.

——, and ——, 1991b: Midlevel vorticity structure of the 10–11 June 1985 squall line. *Mon. Wea. Rev.,* **119,** 3066–3079.

——, and ——, 1993: Kinematics and microphysics of the transition zone of the 10–11 June 1985 squall line. *J. Amos. Sci.,* **50,** 3091–3110.

——, and S. A. Listemaa, 2000: An improved scheme for convective/stratiform echo classification using radar reflectivity. *J. Appl. Meteor.,* **39,** 2129–2150.

Byers, H. R., and R. R. Braham Jr., 1949: *The Thunderstorm*. U.S. Department of Commerce, Weather Bureau, 287 pp.

DeMaria, M., 1985: Linear response of a stratified tropical atmosphere to convective forcing. *J. Atmos. Sci.,* **42,** 1944–1959.

Draine, B. T., and P. J. Flatau, 1994: Discrete-dipole approximation for scattering calculations. *J. Opt. Soc. Amer.,* **11A,** 1491–1499.

Ferranti, L., F. Molteni, C. Brankovic, and T. N. Palmer, 1994: Diagnosis of extratropical variability in seasonal integrations of the ECMWF model. *J. Climate,* **7,** 849–868.

Hartmann, D. L., H. H. Hendon, and R. A. Houze Jr., 1984: Some implications of the mesoscale circulations in tropical cloud clusters for large-scale dynamics and climate. *J. Atmos. Sci.,* **41,** 113–121.

Hashem, M. S., and M. I. Biggerstaff, 1997: Organization of convection in mesoscale systems. Preprints, *28th Conf. of Radar Meteorology,* Austin, TX, Amer. Meteor. Soc., 483–484.

Houghton, H. G., 1968: On precipitation mechanisms and their artificial modification. *J. Appl. Meteor.,* **7,** 851–859.

Houze, R. A., Jr., 1982: Cloud clusters and large-scale vertical motions in the Tropics. *J. Meteor. Soc. Japan,* **60,** 396–409.

——, 1989: Observed structure of mesoscale convective systems and implications for large-scale heating. *Quart. J. Roy. Meteor. Soc.,* **115,** 425–461.

——, M. I. Biggerstaff, S. A. Rutledge, and B. F. Smull, 1989: Interpretation of Doppler weather radar displays of midlatitude mesoscale convective systems. *Bull. Amer. Meteor. Soc.,* **70,** 608–619.

——, B. F. Smull, and P. Dodge, 1990: Mesoscale organization of springtime rainstorms in Oklahoma. *Mon. Wea. Rev.,* **118,** 613–654.

Hristova-Veleva, S. M., 2000: Impact of microphysical parameterizations on simulated storm evolution and remotely-sensed characteristics. Ph.D. dissertation, Texas A&M University, 201 pp.

Iguchi, T., T. Kozu, R. Meneghini, J. Awaka, and K. Okamoto, 2000: Rain-profiling algorithm for the TRMM precipitation radar. *J. Appl. Meteor.,* **39,** 2038–2052.

Johnson, D. E., 1984: Partitioning tropical heat and moisture budgets into cumulus and mesoscale components: Implications for cumulus parameterization. *Mon. Wea. Rev.,* **112,** 1590–1601.

Keenan, T. D., B. Ferrier, and J. Simpson, 1994: Development and structure of a maritime continent thunderstorm. *Meteor. Atmos. Phys.,* **53,** 185–222.

Kummerow, C., 1993: On the accuracy of the Eddington approximation for radiative transfer in the microwave frequencies. *J. Geophys. Res.,* **98,** 2757–2765.

——, W. S. Olson, and L. Giglo, 1996: A simplified scheme for

obtaining precipitation and vertical hydrometeor profiles from passive microwave sensors. *IEEE Trans. Geosci. Remote Sens.,* **34,** 1213–1232.

——, and Coauthors, 2000: The status of the Tropical Rainfall Measuring Mission (TRMM) after two years in orbit. *J. Appl. Meteor.,* **39,** 1965–1982.

Leary, C. A., and R. A. Houze Jr., 1979: The structure and evolution of convection in a tropical cloud cluster. *J. Atmos. Sci.,* **36,** 437–457.

Lin, Y.-L., R. D. Farley, and H. D. Orville, 1983: Bulk parameterization of the snow field in a cloud model. *J. Climate Appl. Meteor.,* **22,** 1065–1092.

Liu, G., 2004: Approximation of single scattering properties of ice and snow particles for high microwave frequencies. *J. Atmos. Sci.,* **62,** 2441–2456.

Malkus, J. S., 1962: Large-scale interactions. *The Sea—Ideas and Observations on Progress in the Study of the Seas, Vol. 1: Physical Oceanography,* M. N. Hill, Ed., Interscience, 88–294.

Marshall, J. S., and W. M. Palmer, 1948: The distribution of raindrops with size. *J. Meteor.,* **5,** 165–166.

McCumber, M., W.-K. Tao, J. Simpson, R. Penc, and S.-T. Soong, 1991: Comparison of ice-phase microphysical parameterization schemes using numerical simulations of tropical convection. *J. Appl. Meteor.,* **30,** 985–1004.

Meneghini, R., J. A. Jones, T. Iguchi, K. Okamoto, and J. Kwiatkowski, 2004: A hybrid surface reference technique and its application to the TRMM precipitation radar. *J. Atmos. Oceanic Technol.,* **21,** 1645–1658.

Mie, G., 1908: Beiträge zur Optik trüber Medien speziell kolloidaler Metallösungen (Contributions to the optics of turbid media, particularly of colloidal metal solutions). *Ann. Phys.,* **25,** 377–445.

Molteni, F., and R. Buizza, 1999: Validation of the ECMWF ensemble prediction system using empirical orthogonal functions. *Mon. Wea. Rev.,* **127,** 2346–2358.

Mugnai, A., E. A. Smith, and G. J. Tripoli, 1993: Foundations for statistical–physical precipitation retrieval from passive microwave satellite measurements. Part II: Emission-source and generalized weighting-function properties of a time-dependent cloud-radiation model. *J. Appl. Meteor.,* **32,** 17–39.

Olson, W. S., C. D. Kummerow, G. M. Heymsfield, and L. Giglio, 1996: A method for combined passive–active microwave retrievals of cloud and precipitation profiles. *J. Appl. Meteor.,* **35,** 1763–1789.

——, ——, Y. Hong, and W.-K. Tao, 1999: Atmospheric latent heating distributions in the Tropics derived from satellite passive microwave radiometer measurements. *J. Appl. Meteor.,* **38,** 633–664.

Panegrossi, G., and Coauthors, 1998: Use of cloud model microphysics for passive microwave-based precipitation retrieval: Significance of consistency between model and measurement manifolds. *J. Atmos. Sci.,* **55,** 1644–1673.

Petty, G. W., 1999: Cloud physical and microwave radiative properties of tropical stratiform precipitation inferred from multichannel microwave radiances. Preprints, *10th Conf. Satellite Meteorology and Oceanography,* Long Beach, CA, Amer. Meteor. Soc., 318–320.

Riehl, H., and J. S. Malkus, 1958: On the heat balance in the equatorial trough zone. *Geophysica,* **6,** 503–538.

——, and J. Simpson, 1979: The heat balance of the equatorial trough zone, revisited. *Contrib. Atmos. Phys.,* **52,** 287–304.

Rutledge, S. A., and P. V. Hobbs, 1984: The mesoscale and microscale structure and organization of clouds and precipitation in midlatitude clouds. Part XII: A diagnostic modeling study of precipitation development in narrow cold frontal rainbands. *J. Atmos. Sci.,* **41,** 2949–2972.

Seo, E.-K., and M. I. Biggerstaff, 2006: Impact of cloud model microphysics on passive microwave retrievals of cloud properties. Part II: Uncertainty in rain, hydrometeor structure, and latent heating retrievals. *J. Appl. Meteor. Climatol.,* **45,** 955–972.

Simpson, J., R. F. Alder, and G. R. North, 1988: A proposed Tropical Rainfall Measuring Mission (TRMM) satellite. *Bull. Amer. Meteor. Soc.,* **69,** 278–295.

Skamarock, W. C., and J. B. Klemp, 1993: Adaptive grid refinement for two-dimensional and three-dimensional nonhydrostatic atmospheric flow. *Mon. Wea. Rev.,* **121,** 788–804.

——, M. L. Weisman, and J. B. Klemp, 1994: Three-dimensional evolution of simulated long-lived squall lines. *J. Atmos. Sci.,* **51,** 2563–2584.

Smith, E. A., A. Mugnai, H. J. Cooper, G. J. Tripoli, and X. Xiang, 1992: Foundations for statistical–physical precipitation retrieval from passive microwave satellite measurements. Part I: Brightness temperature properties of a time-dependent cloud-radiation model. *J. Appl. Meteor.,* **31,** 506–531.

——, X. Xiang, A. Mugnai, and G. J. Tripoli, 1994: Design of inversion-based precipitation profile retrieved algorithm using an explicit cloud model for initial guess microphysics. *Meteor. Atmos. Phys.,* **54,** 53–78.

Spencer, R. W., 1986: A satellite passive 37-GHz scattering-based method for measuring oceanic rain rates. *J. Climate Appl. Meteor.,* **25,** 754–766.

——, B. B. Hinton, and W. S. Olson, 1983: *Nimbus-7* 37 GHz radiances correlated with radar rain rates over the Gulf of Mexico. *J. Climate Appl. Meteor.,* **22,** 2095–2099.

——, H. M. Goodman, and R. E. Hood, 1989: Precipitation retrieval over land and ocean with the SSM/I: Identification and characteristics of the scattering signal. *J. Atmos. Oceanic Technol.,* **6,** 254–273.

Stith, J. L., J. E. Dye, A. Bansemer, and A. J. Heymsfield, 2002: Microphysical observations of tropical clouds. *J. Appl. Meteor.,* **41,** 97–117.

Tao, W.-K., and J. Simpson, 1993: Goddard Cumulus Ensemble Model. Part I: Model description. *Terr. Atmos. Oceanic Sci.,* **4,** 35–72.

——, S. Lang, J. Simpson, and R. Adler, 1993: Retrieval algorithms for estimating the vertical profiles of latent heat release: Their applications for TRMM. *J. Meteor. Soc. Japan,* **71,** 685–700.

Thiele, O. W., Ed., 1987: On requirements for a satellite mission to measure tropical rainfall. NASA Reference Publication 1183, 49 pp.

Toracinta, E. R., D. J. Cecil, E. J. Zipser, and S. W. Nesbitt, 2002: Radar, passive microwave, and lightning characteristics of precipitating systems in the Tropics. *Mon. Wea. Rev.,* **130,** 802–824.

Twomey, S., 1977: *Introduction to the Mathematics of Inversion in Remote Sensing and Indirect Measurements*. Dover, 243 pp.

von Storch, H., and F. J. Zwiers, 1999: *Statistical Analysis in Climate Research*. Cambridge University Press, 484 pp.

Wang, X. L., and H. L. Rui, 1996: A methodology for assessing ensemble experiments. *J. Geophys. Res.,* **101,** 29 591–29 597.

Weinman, J. A., and R. Davies, 1978: Thermal microwave radiances from horizontally finite clouds of hydrometeors. *J. Geophys. Res.,* **83,** 3099–3107.

Wilheit, T. T., 1986: Some comments on passive microwave measurements of rain. *Bull. Amer. Meteor. Soc.,* **67,** 1226–1232.

——, A. T. C. Chang, M. S. V. Rao, E. B. Rodgers, and J. S. Theon, 1977: A satellite technique for quantitatively mapping rainfall rates over the oceans. *J. Appl. Meteor.,* **16,** 551–560.

——, and Coauthors, 1982: Microwave radiometric observations near 19.35, 92 and 183 GHz of precipitation in tropical storm Cora. *J. Appl. Meteor.,* **21,** 1137–1145.

Wu, R., and J. A. Weinman, 1984: Microwave radiances from precipitating clouds containing aspherical ice, combined phase, and liquid hydrometeors. *J. Geophys. Res.,* **89,** 7170–7178.

Zipser, E. J., 1969: The role of organized unsaturated convective downdrafts in the structure and rapid decay of an equatorial disturbance. *J. Appl. Meteor.,* **8,** 799–814.

——, 1977: Mesoscale and convective-scale downdrafts as distinct components of squall-line structure. *Mon. Wea. Rev.,* **105,** 1568–1589.